

Study of Compressible Flow Through a Rectangular-to-Semiannular Transition Duct

Jeffry Foster and Theodore H. Okiishi
Iowa State University
Ames, Iowa

Bruce J. Wendt
Modern Technologies Corporation
Middleburg Heights, Ohio

Bruce A. Reichert
Kansas State University
Manhattan, Kansas

Prepared for
Lewis Research Center
under Grant NAG3-1561



National Aeronautics and
Space Administration

Office of Management

Scientific and Technical
Information Program

1995

STUDY OF COMPRESSIBLE FLOW THROUGH A RECTANGULAR-TO-SEMIANNULAR TRANSITION DUCT

Jeffry Foster and Theodore H. Okiishi
Iowa State University
Ames, Iowa 50011

Bruce J. Wendt
Modern Technologies Corporation
Middleburg Heights, Ohio 44130
and
Bruce A. Reichert
Kansas State University
Manhattan, Kansas 66505

ABSTRACT

Detailed flow field measurements are presented for compressible flow through a diffusing rectangular-to-semiannular transition duct. Comparisons are made with published computational results for flow through the duct.

Three-dimensional velocity vectors and total pressures were measured at the exit plane of the diffuser model. The inlet flow was also measured. These measurements were made using calibrated five-hole probes. Surface oil flow visualization and surface static pressure data were also taken. The study was conducted with an inlet Mach number of 0.786. The diffuser Reynolds based on the inlet centerline velocity and the exit diameter of the diffuser was 3,200,000. Comparison of the measured data with previously published computational results are made.

Data demonstrating the ability of vortex generators to reduce flow separation and circumferential distortion is also presented.

TABLE OF CONTENTS

LIST OF FIGURES	iii
LIST OF TABLES	v
NOMENCLATURE	vi
ACKNOWLEDGMENTS	viii
CHAPTER I. INTRODUCTION	1
CHAPTER II. A REVIEW OF PRIOR INVESTIGATIONS	4
Duct Research	4
Distortion	5
CHAPTER III. EXPERIMENTAL FACILITY	8
Internal Fluid Mechanics Facility	8
Description of Model Hardware	15
CHAPTER IV. INSTRUMENTATION AND MEASUREMENT TECHNIQUES	21
Surface Flow Visualization	21
Pressure Measurements	21
CHAPTER V. INLET FLOW CONDITIONS	26
CHAPTER VI. RESULTS AND DISCUSSION	31
Flow through Baseline Diffuser	31
Effect of Vortex Generators	41
CHAPTER VII. CONCLUSIONS	46
CHAPTER VIII. RECOMMENDATIONS FOR FURTHER RESEARCH	47
BIBLIOGRAPHY	48

LIST OF FIGURES

Figure I.1	Sketch of bifurcated inlet geometry	2
Figure II.1	Graph showing quantities used in distortion calculations	7
Figure III.1	Schematic of modifications to experimental facility	9
Figure III.2	Side view of three dimensional contraction	10
Figure III.3	Sketch of three dimensional contraction	11
Figure III.4	Side view of two dimensional contraction	12
Figure III.5	Schematic of seal in rotating joint in AIP instrumentation duct	14
Figure III.6	Description of coordinate systems for diffusing transition duct TD118	17
Figure III.7	Tapered fin vortex generator geometry	19
Figure III.8	Vortex generator placement	20
Figure IV.1	Schematic of rake probe	22
Figure IV.2	Measurements in inlet plane	23
Figure IV.3	Measurements in aerodynamic interface plane	23
Figure IV.4	Schematic of static tap geometry	24
Figure IV.5	Streamwise static pressure tap locations	25
Figure IV.6	Location of circumferential static taps	25
Figure V.1	Drawing of boundary layer pitot probe	26
Figure V.2	Experimental law-of-the-wall velocity profile measured near bottom wall 3 inches upstream of diffuser inlet	28
Figure V.3	Flow Characteristics in Contraction Sections	29
Figure VI.1	Sketch depicting the three distinct surfaces present in the duct	32
Figure VI.2	Photograph of surface oil flow visualization	33
Figure VI.3	Tracing of surface oil flow visualization	34
Figure VI.4	Static pressure coefficients in axial direction	35
Figure VI.5	Circumferential static pressure coefficients	36
Figure VI.6	Total pressure contours for baseline case	36

Figure VI.7	Cross flow velocities at exit plane for baseline case	38
Figure VI.8	Axial velocities measured at AIP for baseline case	38
Figure VI.9	Anderson and Kapoor's computation of transverse velocities a) Reduced b) Full Navier Stokes Analysis	39
Figure VI.10	Anderson and Kapoors computation of axial velocities a) Reduced b) Full Navier Stokes Analysis	40
Figure VI.11	Surface oil flow visualization behind vortex generators	42
Figure VI.12	Total pressure contours with vortex generator array	43
Figure VI.13	Distortion intensity	44
Figure VI.14	Distortion extent	44
Figure VI.15	Secondary velocities at exit plane with vortex generators	45
Figure VI.16	Axial velocity with vortex generators	45

LIST OF TABLES

Table III.1	Constants before centerbody begins $\tau < 1$	18
Table III.2	Constants after centerbody begins $\tau > 1$	18
Table V.1	Flow conditions at inlet to diffuser	27

NOMENCLATURE

ENGLISH

a, b, c	=	Constants or coefficients
c	=	Vortex generator cord length
C_p	=	Static pressure coefficient
C_{p_o}	=	Total pressure coefficient
D	=	Engine face and diffuser exit diameter
H	=	Boundary layer shape factor (δ_1/δ_2)
h	=	Vortex generator height
K	=	Relaminarization parameter
M	=	Mach number
MPR	=	Multiple-per-revolution distortion parameter
n	=	Exponent
o	=	Vortex generator width
PAV	=	Average total pressure on a circumferential ring
$PAVLOW$	=	Average total pressure for low pressure region
p	=	Static pressure
p_o	=	Total pressure
r	=	Radial distance at diffuser exit
R	=	Radius of engine face and diffuser exit
Re	=	Reynolds number
T	=	Static temperature
u, v, w	=	Velocity components in the cartesian coordinate system
u^+, y^+	=	Law-of-the-wall coordinates
x, y, z	=	Global cartesian coordinate system
x', y', z'	=	Local cartesian coordinate system perpendicular to centerline

GREEK

ΔPC	=	Circumferential pressure difference
τ	=	Dimensionless axial distance x/R
δ	=	Boundary layer thickness
δ_1	=	Displacement thickness
δ_2	=	Momentum thickness
θ^-	=	Extent of distortion
μ	=	Dynamic viscosity
ν	=	Kinematic viscosity
ρ	=	Static density

SUBSCRIPTS

<i>ave</i>	=	average quantity
<i>cl</i>	=	Inlet centerline condition
<i>max</i>	=	Maximum

ACKNOWLEDGMENTS

This research was carried out under NASA grant NAG2-1561. Without the financial support of NASA it would not have been possible. Without the help of others this research never would have been possible. We would especially like to acknowledge the help of Bill Darby, Bob Erbar, Bob Gronski and Howard Roark. All of whom provided invaluable assistance. A very special thanks goes to Art Sprungle whose perseverance and efficiency was essential to keeping the manufacturing portions of this project on schedule.

CHAPTER I

INTRODUCTION

With the rapid growth of international trade in recent years has come a considerable increase in overseas travel. This change has prompted renewed interest in developing a high speed civil transport aircraft and led to the formation of the national High Speed Civil Transport (HSCT) program and the NASA High Speed Research (HSR) program. Previous efforts to design a supersonic civil transport airplane in the United States were abandoned in the early 1970's, because of unresolved concerns about noise, operating cost, and emission of nitrogen oxides. Around that same time a European supersonic transport, the Concorde, was built. It was noisy, inefficient and unprofitable. It is widely believed that the problems that plagued the first attempts at commercial supersonic flight can now be solved.

A critical component of the propulsion system for this high-speed aircraft is each engine inlet. At cruising speed each inlet must decelerate the air from the airspeed of the plane to about Mach 0.4 relative to the compressor face. This is because current compressor technology requires that the airspeed at the inlet be around Mach 0.4. In order to be effective this deceleration must take place without generating large transverse velocity components, flow distortions, and total pressure losses. The inlet can be thought of as two separate flow components in series: the supersonic entrance and the subsonic diffuser. This thesis describes a study of the flow in the subsonic diffuser. However, in order to understand the design of the diffuser, some knowledge of the supersonic entrance is necessary.

Because of the high cruising speed of this aircraft, each engine inlet must be fairly complex. The inlet geometry must be variable in order to pass the proper amount of air into the engine at conditions ranging from standing still on the runway to supersonic cruise. A much larger inlet area is required to allow sufficient airflow to the engine during subsonic flight than during supersonic flight. Another reason why the inlet must have variable geometry is to avoid unstart. Unstart occurs when, during supersonic flight, the

normal shock moves upstream of the geometric throat of the inlet and out the front of the inlet [1]. This can cause compressor stall with consequent loss of thrust.

There are two general types of entrance geometries: axisymmetric and rectangular. A rectangular entrance is being studied for use in the high speed civil transport because it is generally easier to control than an axisymmetric entrance [2]. One design involves a pair of two-dimensional wedges that divide the airflow into two separate streams. The advantage of choosing this bifurcated design over a single wedge is that it can made much shorter without large total pressure losses and flow non-uniformities. A sketch of a bifurcated entrance can be seen in Figure I.1.

At supersonic cruising speeds the rectangular entrance decelerates the air through a series of oblique shocks followed by a terminal normal shock. The airspeed of the flow entering the normal shock is approximately Mach 1.3. A Mach 1.3 normal shock is used, for the best trade off between pressure recovery and shock stability. A higher Mach number would reduce total pressure recovery. A lower Mach number would make maintaining the position of the shock in the throat area difficult.

As with most engineering designs, choosing the rectangular bifurcated inlet has a trade off, the subsonic diffuser in the bifurcated duct is more complex than the subsonic diffuser in an axisymmetric inlet. The diffuser must connect a rectangular throat to a semi-annular

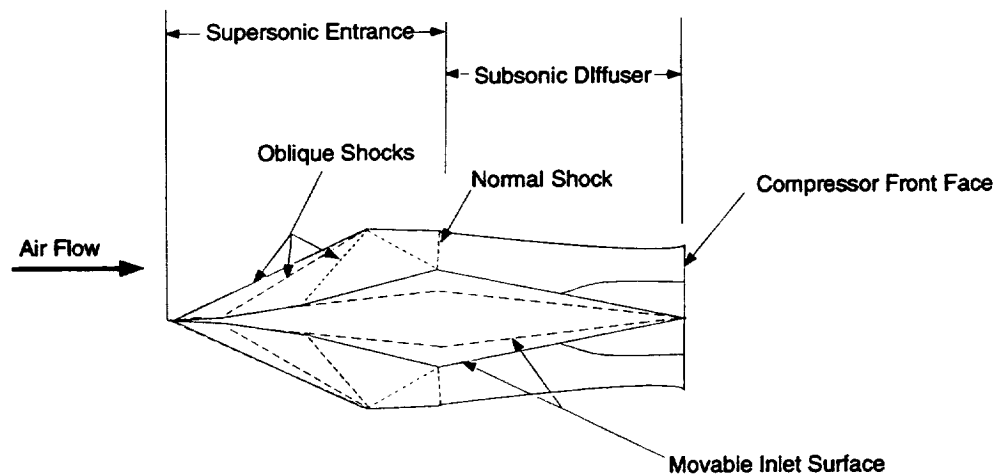


Figure I.1 Sketch of bifurcated inlet geometry

compressor inlet. At the same time the diffuser must decelerate the air from a Mach number of 0.8 to a Mach number of 0.4. The diffuser must accomplish this reduction in airspeed with minimal loss in total pressure, minimal total pressure distortion and without producing large transverse velocity components at the front face of the compressor.

The purpose of the research described in this thesis was to develop a test rig, including instrumentation and a data acquisition and analysis procedure, for experimentally comparing various duct geometries for the HSR diffuser in the Internal Fluid Mechanics Facility (IFMF) at the NASA Lewis Research Center. Tests on one diffuser were used to validate the rig. These experimental results were compared with results from computational work to validate computational fluid dynamics computer codes and are further intended for use in development of high speed civil transport inlet components.

This thesis documents the development and validation of the facility that was built to test rectangular to semiannular diffusing ducts designed for the HSR program. Flow quality data for this facility are presented and the design procedure involved is discussed. A recommended protocol for testing candidate ducts is presented with sample data from the validation duct.

CHAPTER II

A REVIEW OF PRIOR INVESTIGATIONS

Studies on relevant duct flow are reviewed in this section. A discussion of the method used to characterize total pressure distortion is also presented.

Duct Research

In the initial stages of the U.S. attempt in the 60's to design a supersonic transport, a study of the flow through a rectangular to semi-annular transition duct was conducted at Lockheed [3]. Only total pressure data were presented. This duct had a substantial region of separated flow in one corner most likely caused by the streamline curvature of the flow associated with the curvature in the duct's centerline. Total pressure recovery and distortion production were improved by using vortex generators to eliminate the region of separated flow.

More recently, a computational study of the diffuser geometry tested for and described in this thesis was completed at NASA Lewis [4]. Some secondary flows in the form of vortices were predicted in the corners of the duct between the cowl and ramp surfaces. The overall performance of the diffuser was characterized by a predicted loss in pressure recovery of .04 and a maximum predicted DC(60) distortion of .16. Both of these values increased as the inlet Mach number increased. The test data presented later in this thesis are intended to validate these computational results.

A test of a bifurcated supersonic inlet was conducted by Mealson, *et al.* in the 10x10 wind tunnel at NASA Lewis [5]. The subsonic diffuser used by Mealson, *et al.* was similar to the one tested in the IFMF. He found good symmetry between the flows through each of the bifurcated ducts suggesting that the results from only one of the two ducts can be used with some confidence. Mealson, *et al.* also found considerable distortion of the total pressure distribution at the diffuser exit plane.

That no detailed experimental studies on rectangular-to-semiannular diffusers can be found in the literature is one reason this study was being conducted. This thesis provides an experimental data set that can be compared to computational results, and aid also designers of the High Speed Civil Transport inlet in determining an optimum configuration.

Distortion

One goal of this thesis is to provide a method for reducing and reporting the data taken in subsonic diffuser tests. One of the most important quantities considered is total pressure distortion level. A thorough review of distortion literature was completed to determine how best to measure and report distortion.

Spatial distortion in total pressure distribution at the compressor front face can reduce the surge and stall margin of the compressor. Circumferential distortion is almost always detrimental to compressor performance. Radial distortion is less likely to hinder the compressor performance, and is therefore frequently not reported [6].

Distortion results are commonly reported at what is known as the Aerodynamic Interface Plane (AIP). This is the plane of the compressor front and the inlet diffuser exit, and it is where industry standards dictate total pressure recovery and distortion be reported. Because it is sometimes difficult to compare detailed contour plots of total pressure distribution at the AIP, distortion indices were derived to quantify this distortion at the compressor face in global metrics. Since there is no universally accepted distortion index [7], a decision about the type of index to use presently was made.

Because of the potential for detrimental effect of distortion on compressor performance, a viable distortion index must provide enough information to determine compatibility of the inlet diffuser with the compressor. The goal of every distortion index proposed is to provide enough information in only a couple of numbers to decide if the inlet and compressor are compatible. Thus a reliable measure of the intensity, circumferential extent, and multiple-per-rev pattern of the distortion are needed [7].

Each of the distortion concerns mentioned above has a specific reason for being important. Intensity is a measure of the magnitude of the distortion, and is important because large total pressure deficits encourage compressor stall. The circumferential extent of the distortion is important because, compressors have a limit to how large an area of circumferential distortion can be before the blades reach a steady response to the low pressure [8]. This is also the reason the multiple-per-rev information is important, since a blade traveling through several deficits, may be affected differently than if it traveled through only one deficit.

Based on these considerations the best method of reporting distortion appears to be the one described in the Society of Automotive Engineer's Aerospace Recommended Practices (ARP) report 1420 [9]. This report presents a general means for describing distortion in a way that allows compatibility between the inlet diffuser and compressor to be assessed. The primary advantage of this method over others that meet the requirements of a good distortion descriptor was its generality.

To insure that diffuser test measurements were acquired in a way that the distortion descriptors recommended in ARP 1420 could be used, SAE Aerospace Information Report (AIR) 1419 was referred to. This reports suggests that a forty probe rake, eight arms with five probes on each arm, be used as the minimum amount of instrumentation for measuring distortion [10]. Because more than forty data points were deemed necessary to achieve the resolution of the diffuser exit flow field desired, it was decided that more than forty data points per plane would also be used to calculate the distortion index. Another reason for using more points to calculate distortion is that the bifurcated design creates a region of distortion in the plane of the splitter plate. AIR 1419 recommends that, because of this unique characteristic in bifurcated designs, care be taken to avoid allowing the splitter plane distortion to underpredict the performance of the inlet.

The definitions for the intensity, extent and multiple-per-rev patterns are indicated by

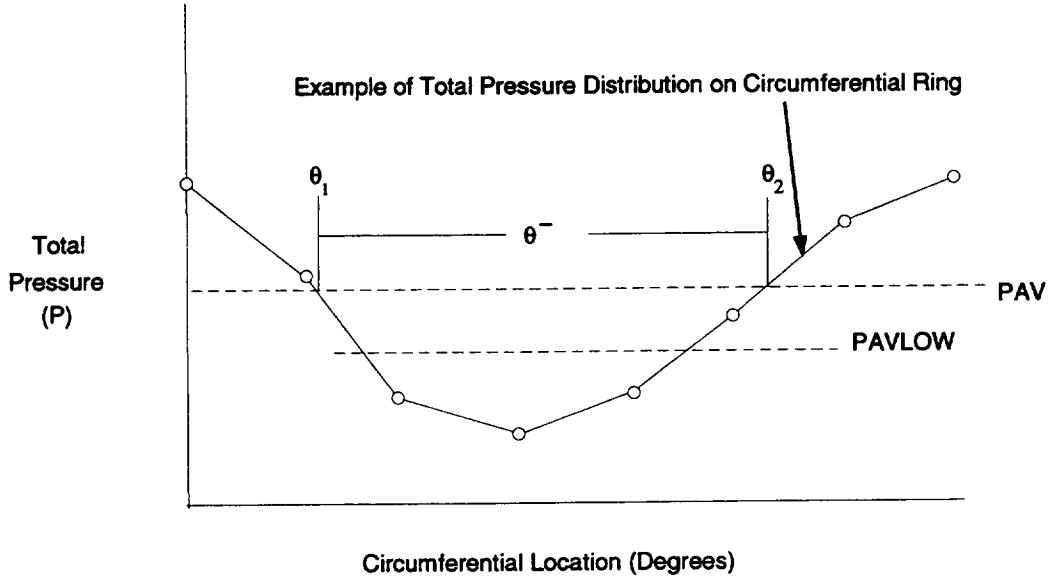


Figure II.1 Graph showing quantities used in distortion calculations

the relations [9]:

$$Intensity = \left(\frac{\Delta PC}{P} \right)_i = \frac{(PAV)_i - (PAVLOW)_i}{(PAV)_i}$$

$$where : (PAV)_i = \frac{1}{360} \int_0^{360} P(\theta)_i d\theta = \text{ring average pressure} \quad (II.1)$$

where $P(\theta)$ is a linear fit between data points

$$(PAVLOW)_i = \frac{1}{\theta_i^-} \int_{\theta_i^-} P(\theta)_i d\theta$$

$$Extent = \theta_i^- = \sum_{K=1}^Q \theta_{ik}^- \quad (II.2)$$

For figure shown $\theta_i^- = \theta_{2i} - \theta_{1i}$

$$Multiple - per - rev = (MPR)_i = \frac{\sum_{k=1}^Q \left(\left(\frac{\Delta PC}{P} \right)_{ik} \theta_{ik}^- \right)}{\max \left(\left(\frac{\Delta PC}{P} \right)_{ik} \theta_{ik}^- \right)} \quad (II.3)$$

CHAPTER III

EXPERIMENTAL FACILITY

In this chapter the Internal Fluid Mechanics Facility and the diffuser model hardware are described.

Internal Fluid Mechanics Facility

To study diffusing ducts with a rectangular-to-semiannular cross-section transition, major modifications had to be made to the existing hardware used to test ducts in the NASA-Lewis Internal Fluid Mechanics Facility. Six major components had to be designed and fabricated to accommodate the rectangular-to-semiannular transition duct geometry. These components are a circular-to-square contraction, a two-dimensional-converging nozzle, a cross section transition duct, a new test duct, an instrumentation duct, and a flexible steel connection hose. A schematic diagram of the facility and the new pieces of hardware can be seen in Figure III.1. The original design of the IFMF was documented by Porro, *et al.*[11]. This design was used as the baseline for the redesign effort. The original design had good flow quality in the test section with no secondary flows. The turbulence intensity was measured to be .65%. Since previous duct experiments in this facility have been successful, these flow characteristics were used as a targets the flow quality in the modified IFMF.

As was mentioned previously, the design of the new components for the IFMF was a major part of this study; therefore, the process that was used to design the new parts for the IFMF are described. For all of the new pieces the major design constraints were flow quality, size, ease of manufacturing and cost.

Settling Chamber

The settling chamber used was the same one that was used for previous duct studies at NASA Lewis. The primary function of the settling chamber is to provide a uniform flow to the test section. The air was drawn into the chamber from the test cell through a

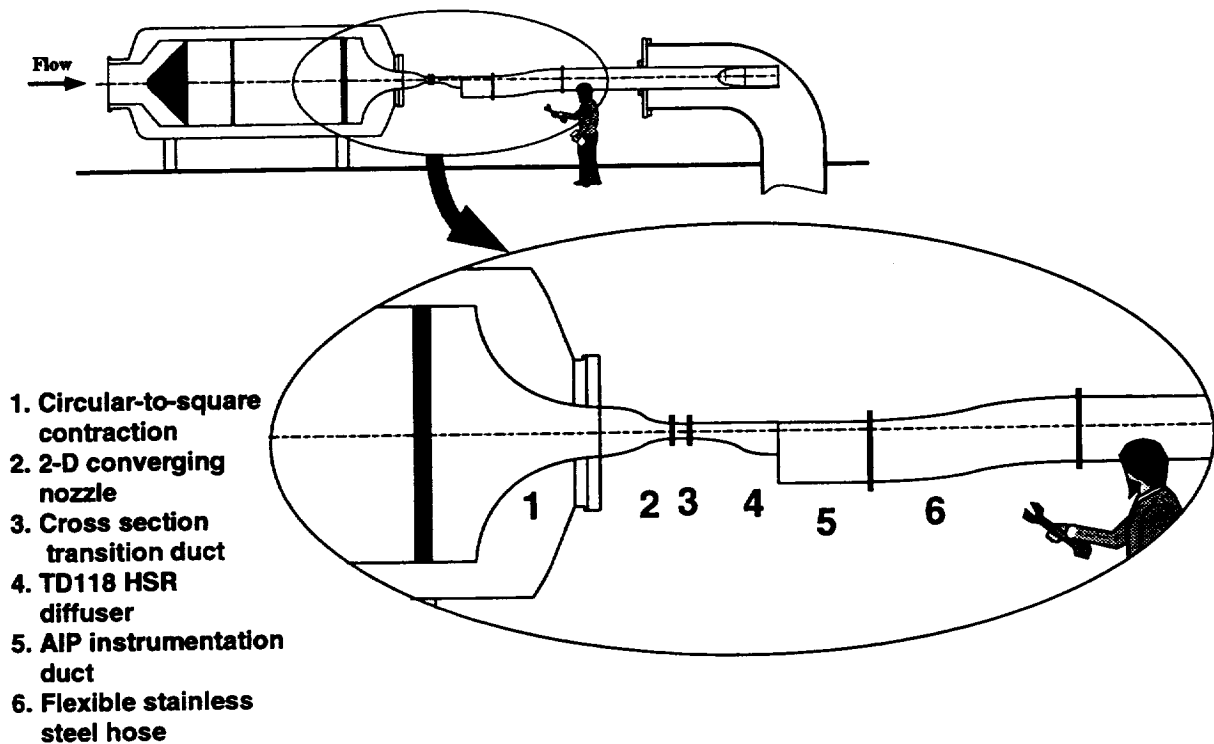


Figure III.1 Schematic of modifications to experimental facility

bellmouth opening. A perforated spreader cone immediately inside the opening assured a thoroughly mixed flow. A course mesh screen located in the middle of the plenum reduced the mean flow nonuniformities. A honeycomb screen near the contraction reduced the large scale turbulence fluctuations. Immediately downstream of this screen was the new circular-to-rectangular contraction.

Contraction

The two parts that make up the contraction of the flow path from the plenum to the test section entrance are the three-dimensional-round-to-square contraction in the plenum, and the two-dimensional-square-to-rectangular nozzle outside the plenum. The round-to-square contraction inside the plenum has an area reduction ratio of 32 (64 inch diameter circle to a 10 inch square). It consists of four sheets of aluminum that were rolled to the proper contour and welded together. The overall length of the contraction section is 31 inches. That length includes a 27 inch radius contraction followed by a four inch long ten by ten inch constant area section.

Because the contractions had to be designed, manufactured, and delivered in four months, ease of manufacturing was an extremely important design consideration. This criterion was met by giving the three-dimensional contraction a constant radius of curvature. An additional constraint placed on the three-dimensional contraction was to fit into the existing plenum. This meant that it had to be 31 inches long and 64 inches in diameter at the inlet. It was impossible to avoid the square shape of the contraction outlet, because of the shape of the ducts to be tested, despite the fact that square corners tend to cause undesirable secondary flows to develop [12]. Design curves previously created by other researchers were consulted in the design process [13,14]. However, due to geometric constraints the design used was shorter than the curves recommended. This was unavoidable. However, the previous IFMF contraction was shorter, in terms of contraction ratio for a given length, and still delivered good flow quality.

Figure III.2 shows the three-dimensional contraction attached to the plenum. For this contraction $\rho=32$ inches, $d=10$ inches, $a=27$ inches and $b=4$ inches. In this sketch a represents the radius of curvature of the contraction and b represents the length for which the flow path has a constant area, ρ is the diameter of the plenum, and d is the width of the square contraction exit.

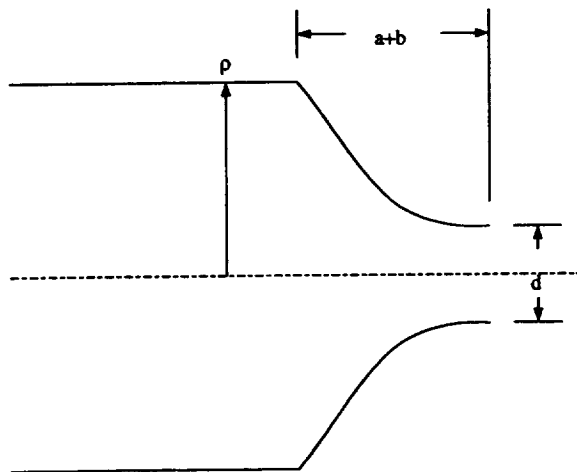


Figure III.2 Side view of three dimensional contraction

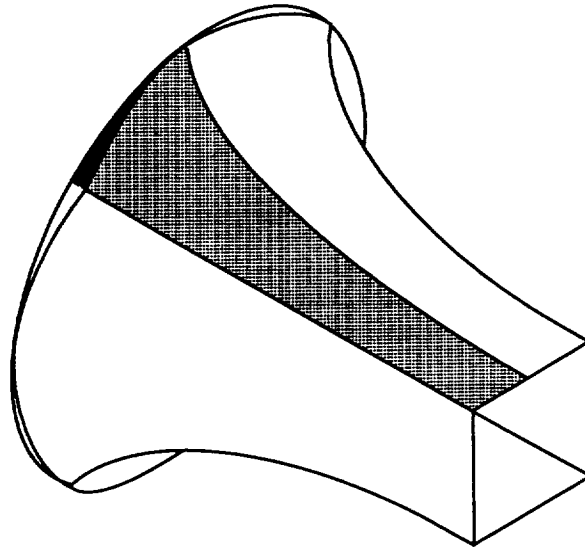


Figure III.3 Sketch of three dimensional contraction

Assembled the three dimensional contraction has scallops at the upstream end, due to the fact that there is no compound curvature in the walls. A sketch of the contraction can be seen in Figure III.3

The second part of the contraction is the two-dimensional converging nozzle located immediately outside of the plenum downstream of the three-dimensional contraction. It has a contraction area ratio of five. Together the circular-to-square contraction and the two-dimensional converging nozzle have an area contraction ratio of 150. The contour of each of the two sides of the two-dimensional nozzle is a circular arc having the same constant radius of curvature. (A drawing of the nozzle can be seen in Figure III.4.) This contour was chosen over a spline curve because the differences between the circular arc and a similar spline curve were minimal, and the spline curve contour would have cost more and taken longer to manufacture than the circular arc. This nozzle is eighteen inches long.

In two dimensional contractions like the one used, relaminarization of the boundary layer has been observed [15]. An acceleration parameter useful for predicting boundary layer relaminarization is $K = \frac{\nu}{U_e^2} \frac{\partial U_e}{\partial x}$ [16]. When K reaches 3×10^{-6} reverse transition can take place. From a one-dimensional analysis the largest computed value for this contraction

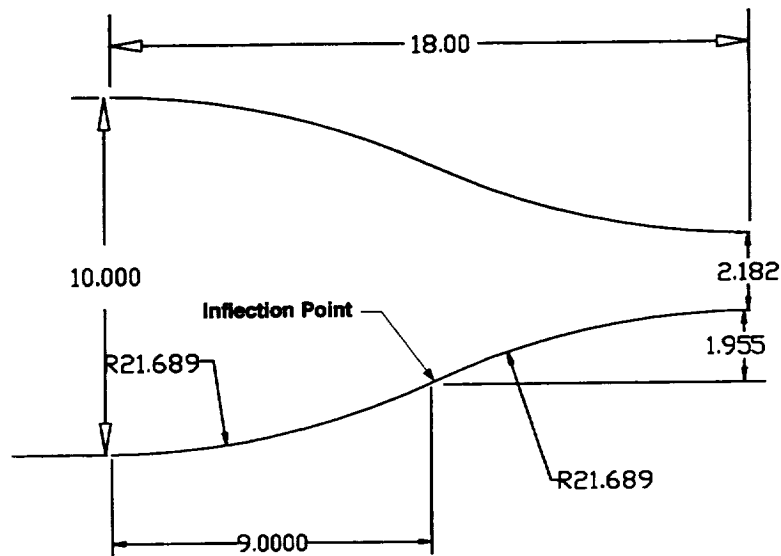


Figure III.4 Side view of two dimensional contraction

was 1.4×10^{-6} . This indicates that it is unlikely that reverse transition would take place in this nozzle, and if it did it the boundary layer would probably quickly return to a turbulent state once the pressure gradient was reduced [17].

Following the two-dimensional nozzle there is a six-inch long transition duct that was needed for the baseline duct that was tested for this study. It was required, because the cross section of the baseline diffuser entrance is super-elliptical, while the cross section of the nozzle exit is rectangular. This transition duct changes the flow cross section from one with four square corners to one with two square and two rounded corners. The transition duct contains several ports that permit flow measurements to be made upstream of the td118 diffuser.

Test Section

The Internal Fluid Mechanics Facility is able to accommodate changes in several geometric parameters of the model ducts to be tested. There is some flexibility in the amount of offset allowed between the inlet and exit planes, since the AIP duct can be moved up and down several inches to accommodate these offsets. The length of the test section can also be varied enough to test any duct that would be a practical candidate for the HSR project. The only parameters that must remain constant are the exit plane cowl

diameter, and the inlet plane width. The diameter of the exit plane must be ten inches. The inlet must also be ten inches wide.

The baseline diffuser geometry tested during this study is described in detail later in this chapter.

AIP Instrumentation Duct

The Aerodynamic Interface Plane (AIP) instrumentation duct is located immediately downstream of the test duct. The primary function of the instrumentation duct is to hold rake probes at the exit plane of the test duct. The instrumentation duct is primarily made of a 36 inch long aluminium pipe with a 10 inch inside diameter. The flow path in the duct is semi-annular and matches the test diffuser exit cross section. A ring in the pipe wall beginning at about 2.5 inches downstream from the test diffuser exit and extending 4 inches further downstream is allowed to rotate freely. This ring is designed to hold rakes of probes used to measure flow quantities at the exit of the test diffuser. The diameter of the hub portion of the instrumentation duct is 4 inches and also has a rotating wall in the same axial position as the outer wall ring. The semiannulus is completed by two flat plates that bisect the outside pipe and are 24 inches long.

The duct is capable of holding two rakes of five-hole probes that are separated circumferentially by ninety degrees. These rakes are rotated with the rotating rings to reach any portion of the test diffuser exit area. The rakes do not pass directly through the center of the duct, but are offset from the center slightly to allow measurements to be taken near the flat wall of the semi-annulus.

Because the static pressure in the AIP duct is less than atmospheric, the interface between the rotating and non-rotating portions of this duct must be sealed. This was partially achieved by placing thin strips of teflon tape into the bearing space formed by the mating pieces of the instrumentation duct. Vacuum grease was placed in the groove to complete the seal and aid in lubrication. To completely seal the interface an o-ring was placed on top of the joint between the rotating and stationary parts. When the facility was

being run, this o-ring was pushed into this joint by the pressure difference between test cell and the inside of the duct, and prevented any leakage from taking place. Figure III.5 shows a schematic of this joint. The flow wetted surface of this joint was sanded smooth to the touch. This minimized any disturbance of the flow induced by the interface between the rotating and stationary parts of the duct.

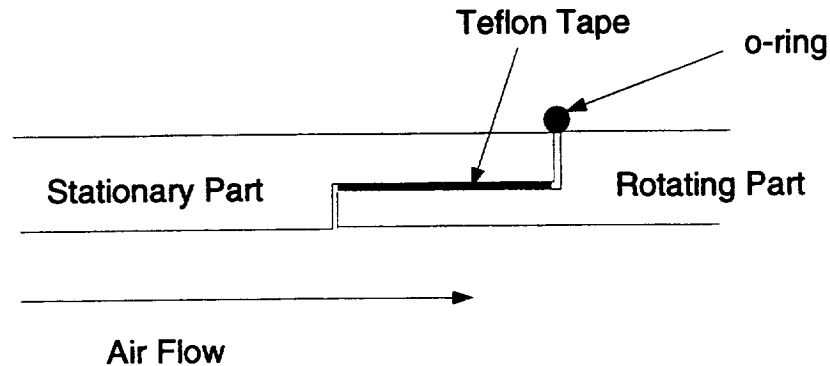


Figure III.5 Schematic of seal in rotating joint in AIP instrumentation duct

Downstream of the instrumentation duct is a flexible braided stainless steel hose. With the original rigid flow path design, the plenum had to be raised or lowered to accommodate different amounts of offsets between inlet and exit planes of test ducts. With the flexible hose, different offsets are handled easily. The hose is connected to the exhaust system.

Exhaust Section

The other major portion of the existing equipment used is the exhaust section of the IFMF. The primary parts of this section are a circular pipe, a mass flow plug and a sub-atmospheric pressure exhaust. The mass flow plug in the circular pipe controls the flow through the test section. The flow past the mass flow plug is choked, and thus the facility operates at constant flow even when conditions in the exhaust plenum change. Flow is simply dumped into the laboratory wide sub-atmospheric pressure exhaust system after passing the mass flow plug.

Seals

In addition to the rotating portion of the instrumentation duct, the interface between each mating piece must contain a seal. Each interface upstream of the AIP was sealed by using a rubber o-ring in the flange of one of the mating parts. No o-rings are necessary for ducts tested, because there is one in the upstream section, and one in the AIP instrumentation duct. This reduces the cost of making new model ducts.

Description of Model Hardware

Diffusing Transition Duct Geometry

The duct tested in this study, named td118 by researchers at NASA, was designed to be as short as possible. A shorter diffuser provides savings in weight, but has a greater streamline curvature which increases the possibility of secondary and separated flows developing. This duct starts with a rectangular cross-section with rounded corners on top, square corners below, and ends up with a semiannular cross-section. The centerbody that forms the inner surface of the annulus begins one engine face radius downstream of the inlet of the test duct. The geometry for this duct is described by a centerline and a series of super-ellipses. The centerline is described by a series of polynomials, while the super-ellipses are defined by an elliptic equation containing polynomials.

The centerline of the duct starts at the center of the bottom of the duct at the inlet and continues along the bottom surface of the duct until the centerbody begins at which point the centerline becomes the center of the centerbody. The parametric equations that describe the centerline of the duct are as follows:

$$\begin{aligned}
 x_{cl}/R &= c_{0,0} + c_{0,1}\tau + c_{0,2}\tau^2 + c_{0,3}\tau^3 + c_{0,4}\tau^4 + c_{0,5}\tau^5 \\
 y_{cl}/R &= c_{1,0} + c_{1,1}\tau + c_{1,2}\tau^2 + c_{1,3}\tau^3 + c_{1,4}\tau^4 + c_{1,5}\tau^5 \\
 z_{cl}/R &= c_{2,0} + c_{2,1}\tau + c_{2,2}\tau^2 + c_{2,3}\tau^3 + c_{2,4}\tau^4 + c_{2,5}\tau^5
 \end{aligned}
 \tag{III.1}$$

The parameter τ is the distance x/R from the inlet, and R is the outside radius of the annulus at the duct exit.

The equation that describes the super-ellipse that makes the wall of the duct is in a plane perpendicular to the centerline (y', z'):

$$\left(\frac{y'/R}{a_o}\right)^n + \left(\frac{z'/R}{b_o}\right)^n = 1 \quad (\text{III.2})$$

Where the parameters a_o , b_o , and n are functions of τ . The polynomials that define these constants are

$$\begin{aligned} a_o &= c_{3,0} + c_{3,1}\tau^1 + c_{3,2}\tau^2 + c_{3,3}\tau^3 + c_{3,4}\tau^4 + c_{3,5}\tau^5 \\ b_o &= c_{4,0} + c_{4,1}\tau^1 + c_{4,2}\tau^2 + c_{4,3}\tau^3 + c_{4,4}\tau^4 + c_{4,5}\tau^5 \\ n &= c_{5,0} + c_{5,1}\tau^1 + c_{5,2}\tau^2 + c_{5,3}\tau^3 + c_{5,4}\tau^4 + c_{5,5}\tau^5 \end{aligned} \quad (\text{III.3})$$

Similarly the equation for the centerbody is:

$$\left(\frac{y'/R}{a_i}\right)^n + \left(\frac{z'/R}{b_i}\right)^n = 1 \quad (\text{III.4})$$

with parameters a_i , and b_i defined by

$$\begin{aligned} a_i &= c_{6,0} + c_{6,1}\tau^1 + c_{6,2}\tau^2 + c_{6,3}\tau^3 + c_{6,4}\tau^4 + c_{6,5}\tau^5 \\ b_i &= c_{7,0} + c_{7,1}\tau^1 + c_{7,2}\tau^2 + c_{7,3}\tau^3 + c_{7,4}\tau^4 + c_{7,5}\tau^5 \end{aligned} \quad (\text{III.5})$$

The orientation of the two coordinate systems and the relationship between the centerline and the super-ellipses can be better seen in figure III.6.

The constants in the above equations can be broken up into two groups. One group is used prior to the start of the centerbody, while another group is used after the centerbody begins. The constants can be found in Tables III.1 and III.2.

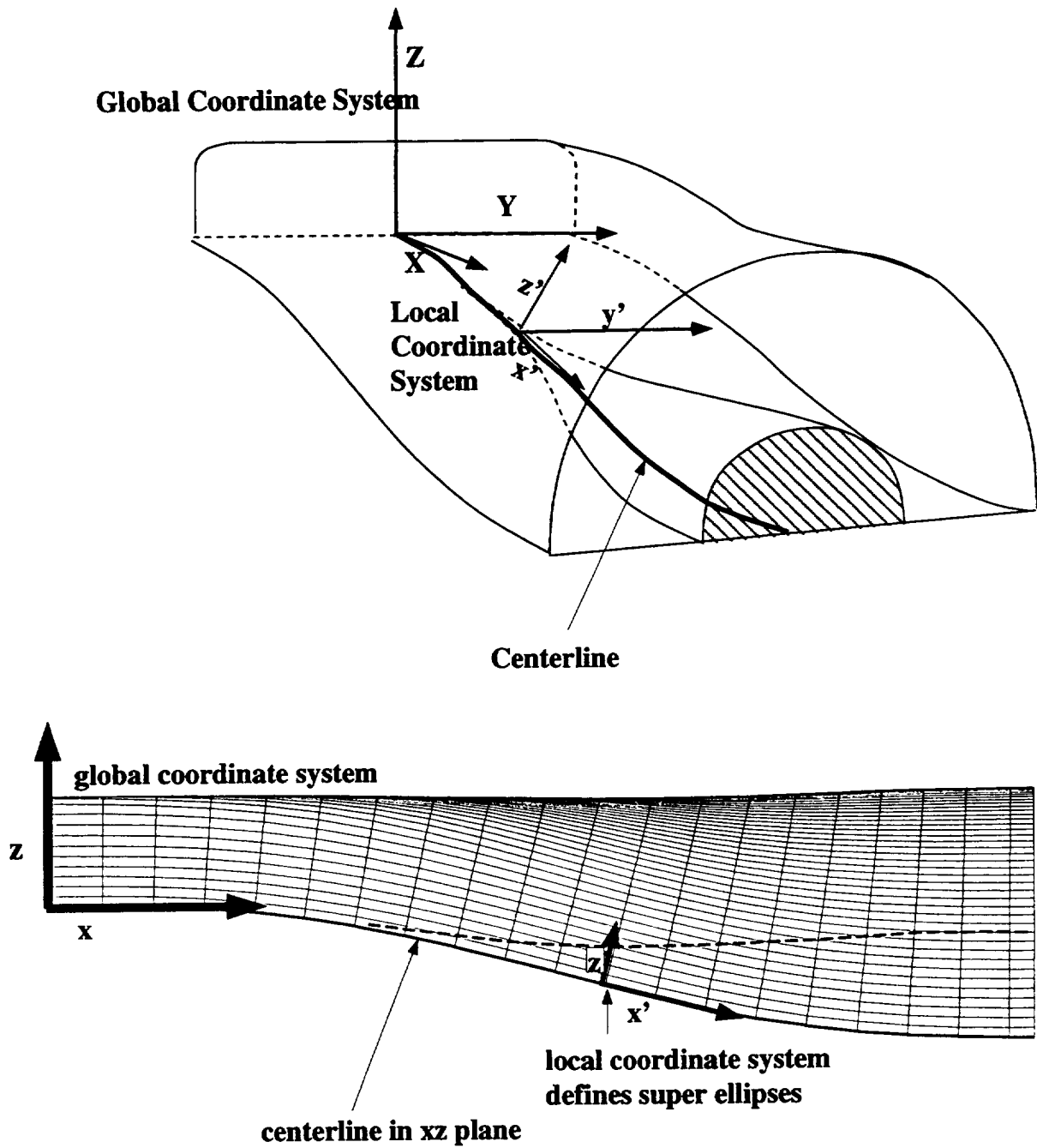


Figure III.6 Description of coordinate systems for diffusing transition duct TD118

Table III.1 Constants before centerbody begins $\tau < 1$

$$0 \leq \tau \leq 1$$

$$j = \dots$$

	0	1	2	3	4	5
0	0	1	0	0	0	0
1	0	0	0	0	0	0
2	0	0	0	-0.08807312	0.03802742	-0.003302742
3	1	0	0	0	0	0
4	0.436332	0	0	0.08807312	-0.03302742	0.003302742
5	20	-20.5	8.625	-1.59375	0.109375	0
6	0	0	0	0	0	0
7	0	0	0	0	0	0

Table III.2 Constants after centerbody begins $\tau > 1$

$$1 \leq \tau \leq 4$$

$$j = \dots$$

	0	1	2	3	4	5
0	0	1	0	0	0	0
1	0	0	0	0	0	0
2	0	0	0	-0.08807312	0.03302742	-0.003302742
3	1	0	0	0	0	0
4	0.436332	0	0	0.08807312	-0.03302742	0.003302742
5	20	-20.5	8.625	-1.59375	0.109375	0
6	-0.2305185	0.7881481	-0.9851852	0.5418519	-0.1231481	0.009851852
7	-0.2305185	0.7881481	-0.9851852	0.5418519	-0.1231481	0.009851852

Vortex Generator Array

An array of tapered fin vortex generators were installed in the duct to control secondary flow and improve diffuser performance. (For the rest of the thesis most lengths will be nondimensionalized by the engine face diameter, D). This type of vortex generator array has been used successfully in other ducts [18]. The vortex generators used had a chord length of $c/D = 0.180$, a height of $h/D = 0.0469$, and an offset width of $o/D = 0.0508$. The geometry can be seen in Figure III.7.

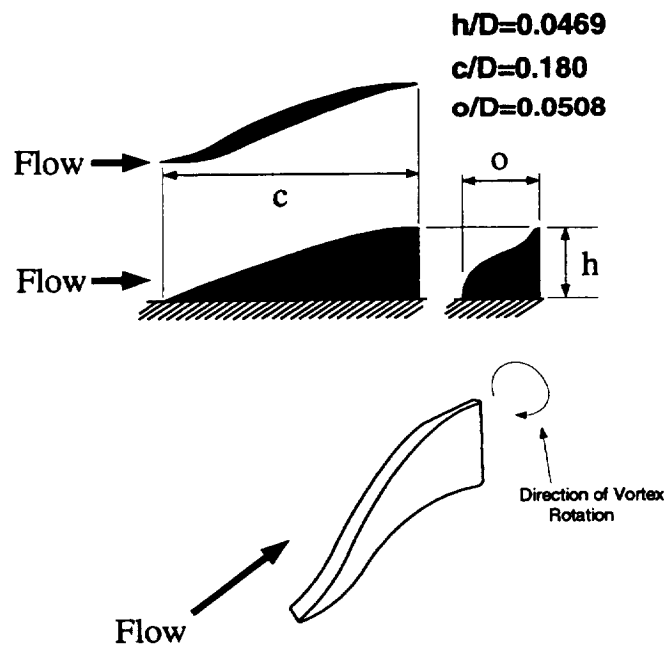


Figure III.7 Tapered fin vortex generator geometry

Two pairs of these vortex generators were placed on the ramp surface of the duct at a $y/D = .25$ on either side of the centerline. The distance from the diffuser inlet to the center of the vortex generators was $x/D = .7$, and they were spaced $y/D = .05$ apart. The layout of the vortex generators on the duct surface can be seen in Figure III.8.

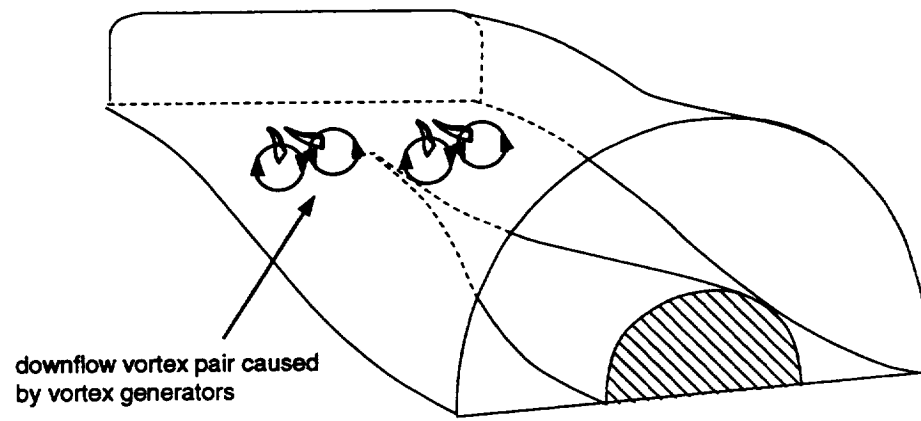


Figure III.8 Vortex generator placement

CHAPTER IV INSTRUMENTATION AND MEASUREMENT TECHNIQUES

Several techniques were used to measure the flow field. Surface flow visualization provided a quick qualitative view of the flow field. Detailed five hole probe data and static pressure data were acquired in to quantify the aerodynamic performance of the duct.

Surface Flow Visualization

The streamlines in the boundary layer on the surface of the duct were visualized with a fluorescent oil on the duct surface. This technique was used to identify regions of time averaged separated flow, and boundary layer cross flows. The method is sensitive to flow unsteadiness. Also the mean local velocity must be high enough to generate wall shear stresses that are capable of overcoming the surface tension of the oil drops.

The fluorescent oil was made by mixing a fluorescent powder and petroleum based lubricating oil. The mixture was thinned slightly by adding mineral oil. It was applied to the surface of the duct in a series of dots that formed a grid on the duct. The duct was then installed in the facility and the facility was run at test conditions for five minutes. The facility was then shut down and the duct was removed. Photographs of the resulting streaklines were taken under black lights, using an ultraviolet lens filter. Tracings of the streaklines were also made by placing white blotter paper, that had previously been cut to fit the contours of the duct, on the duct surfaces that had been covered with oil. The fluorescent oil stains on the paper showed the same pattern as the surface streaklines. This method was used previously on studies in a diffusing S-duct with considerable success [19].

Pressure Measurements

The test diffuser was instrumented to obtain numerous pressure measurements. Total and static pressures in the flow field were measured at the inlet and AIP using five-hole probes. Surface static pressures were measured with surface pressure taps.

Five hole probe measurements

The test diffuser inlet and exit flow fields were investigated using calibrated five hole probes. These probes collected pressure data that was used to calculate three dimensional velocity vectors, and the total and static pressures. Three inches upstream of the inlet, a calibrated probe was traversed across the plane there at the centerline near the side wall and at .25 inch intervals out to 1.37 inches from the side wall (see Figure IV.2.) Measurements were concentrated in the corner, because it was felt that if any secondary flows were present, they would most likely be there. In the exit plane (AIP) measurements were taken at increments of .16 inches in the radial direction, and 5 degrees in the circumferential direction (see Figure IV.3). These probes were used in the nonnulling mode, as described by Reichert and Wendt [20].

The probes used were custom built and had a tip diameter of .063 inches with a tip angle of 45 degrees. The rakes used in the exit plane surveys had a diameter of .25 inches. The probes were placed on the rake at one inch intervals (see Figure IV.1.) This distance

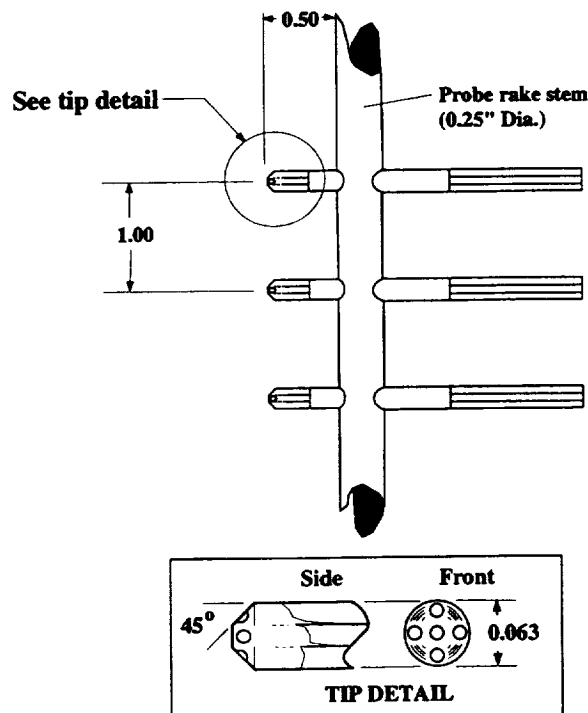


Figure IV.1 Schematic of rake probe

was adequate to insure that there were no interference effects between adjacent probes [21]. The rakes were aligned in the duct in such a way that the center of the rake probe passes through a point offset .125 inches from the center of the instrumentation duct. This was done to allow measurements to be taken along the flat portion of the semiannulus.

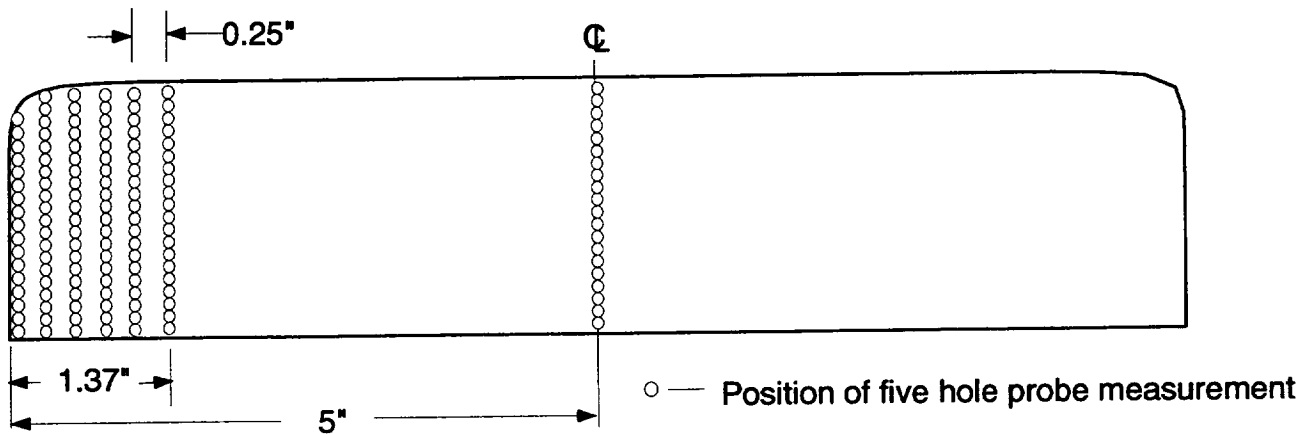


Figure IV.2 Measurements in inlet plane

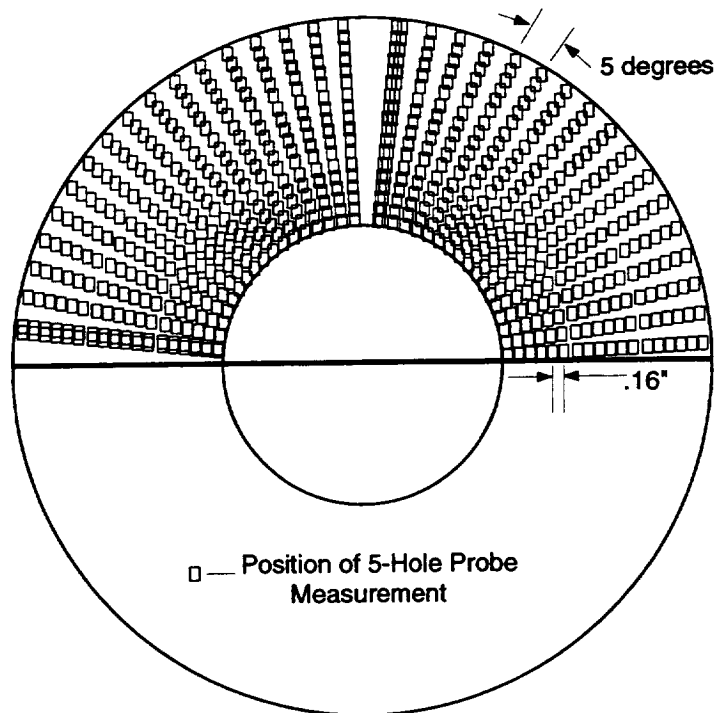


Figure IV.3 Measurements in aerodynamic interface plane

Surface static pressure measurements

One hundred and five static pressure taps were installed on the surface of the test diffuser. Many of these taps were formed during the stereo lithography process used to produce the diffuser. These holes were .020 inches in diameter. A .125 inch hole was bored halfway through the duct from the outside and plugged with a tube having an inside diameter of .08 inches. Epoxy was placed outside the duct to seal the area between the tube and the duct. A sketch of the tap geometry can be seen in Figure IV.4.

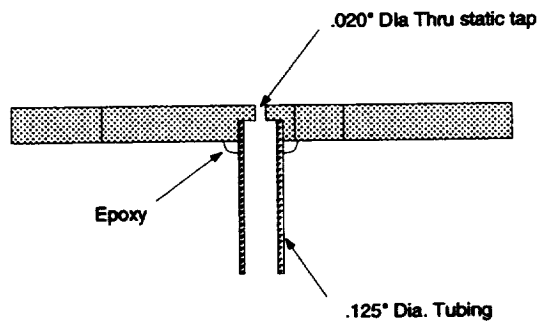


Figure IV.4 Schematic of static tap geometry

The static taps were located in three streamwise lines, and three circumferential planes. The streamwise lines ran the length of the duct. One line ran down the center of the top of the duct. One ran down the center of the bottom of the duct. A third line ran along the bottom of the duct at a position that was halfway between the outer and inner radii of the annulus. These tap locations can be seen in Figure IV.5, most of the holes were one inch apart. The circumferential taps were located in planes at $x/D=.2$, $x/D=1.0$, and $x/D=1.8$ (Figure IV.6). The taps were around one half of the duct, also spaced one inch apart.

Arrangement of Streamwise Distributions of Static Pressure Taps on Model Duct

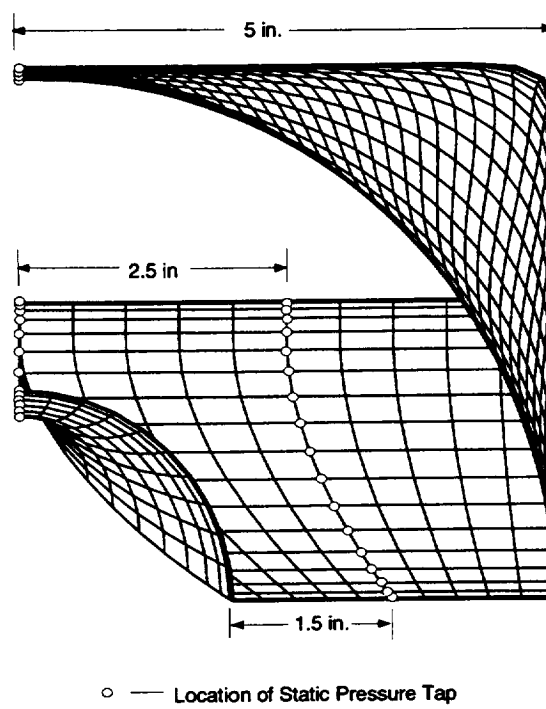


Figure IV.5 Streamwise static pressure tap locations

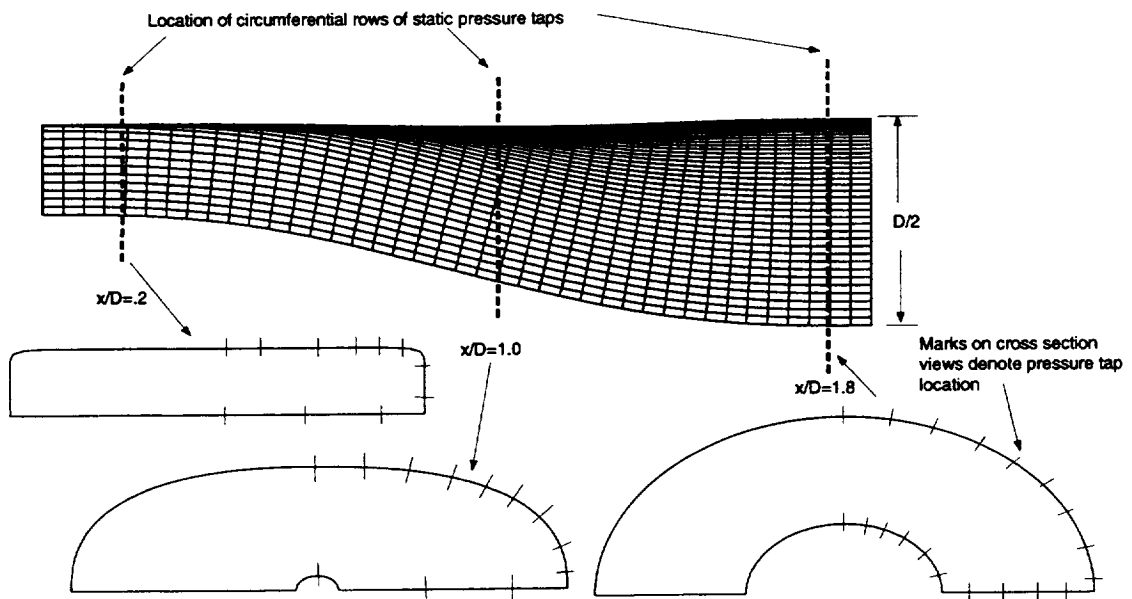


Figure IV.6 Location of circumferential static taps

CHAPTER V

INLET FLOW CONDITIONS

Test inlet flow conditions were obtained at a cross section plane three inches upstream of the inlet to the test diffuser. Boundary layer measurements were taken using a pitot probe with a .010 inch diameter tip (see Figure V.1). All reported tests were conducted with an inlet centerline Mach number of 0.786. The Reynolds number, based on the inlet width and centerline velocity, was 3.2×10^6 . All boundary layer quantities presented here are from measurements on the centerline at the bottom of the diffuser inlet. It should be noted though that measurements near the corners of the diffuser, near both the top and bottom walls, were nearly identical to those on the centerline.

A thin turbulent inlet boundary layer existed at the inlet to the diffuser. The boundary layer thickness, δ , was defined as being from the wall to where 99% of the free stream velocity was achieved. The displacement thickness, δ_1 , momentum thickness, δ_2 , and

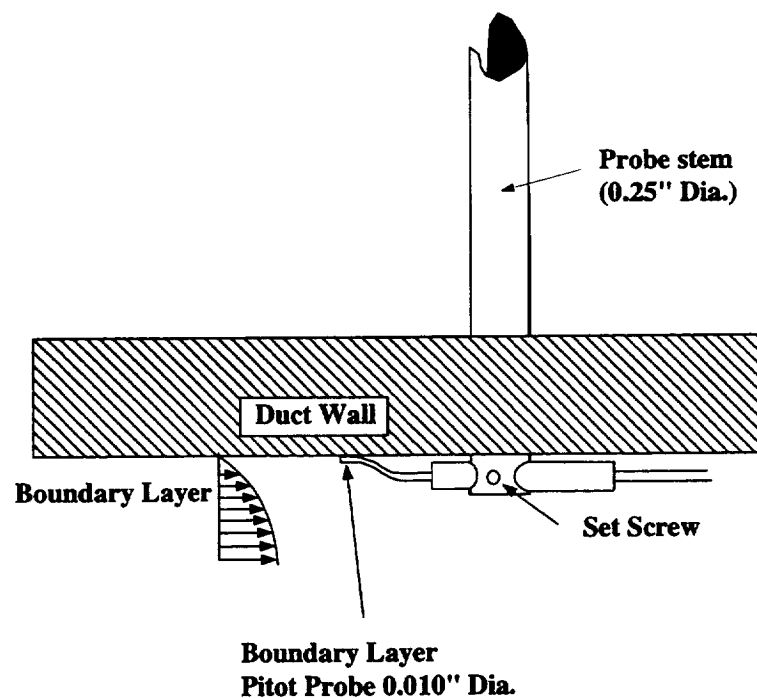


Figure V.1 Drawing of boundary layer pitot probe

shape factor, H , used to further quantify the inlet flow conditions, are defined by Equations V.1–V.3. These boundary layer parameters were calculated by numerically integrating the survey data using the trapezoidal numerical integration technique. The inlet flow conditions are listed in Table V.1.

$$\delta_1 = \int_0^{z_1} \left(1 - \frac{\rho u}{\rho_{cl} u_{cl}} \right) dz \quad (\text{V.1})$$

$$\delta_2 = \int_0^{z_1} \frac{\rho u}{\rho_{cl} u_{cl}} \left(1 - \frac{u}{u_{cl}} \right) dz \quad (\text{V.2})$$

$$H = \frac{\delta_1}{\delta_2} \quad (\text{V.3})$$

The centerline inlet velocity profile, plotted in nondimensional law-of-the-wall coordinates, is shown in Figure V.2. The friction velocity, used to define law-of-the-wall coordinates, was not measured but instead was chosen to provide the best approximation of the linear profile region of the test data to the law-of-the-wall logarithmic function defined by Equation V.4. The data agree with the behavior predicted by the equation, indicating the boundary layer is turbulent.

Table V.1 Flow conditions at inlet to diffuser

Inlet Parameter	Measured Value
M_{cl}	0.786
Re_{cl}	3,200,000
$(\delta/D) \times 100$	0.800
$(\delta_1/D) \times 100$	0.135
$(\delta_2/D) \times 100$	0.089
H	1.52

Inlet Boundary Layer Plotted In Law of The Wall Coordinates

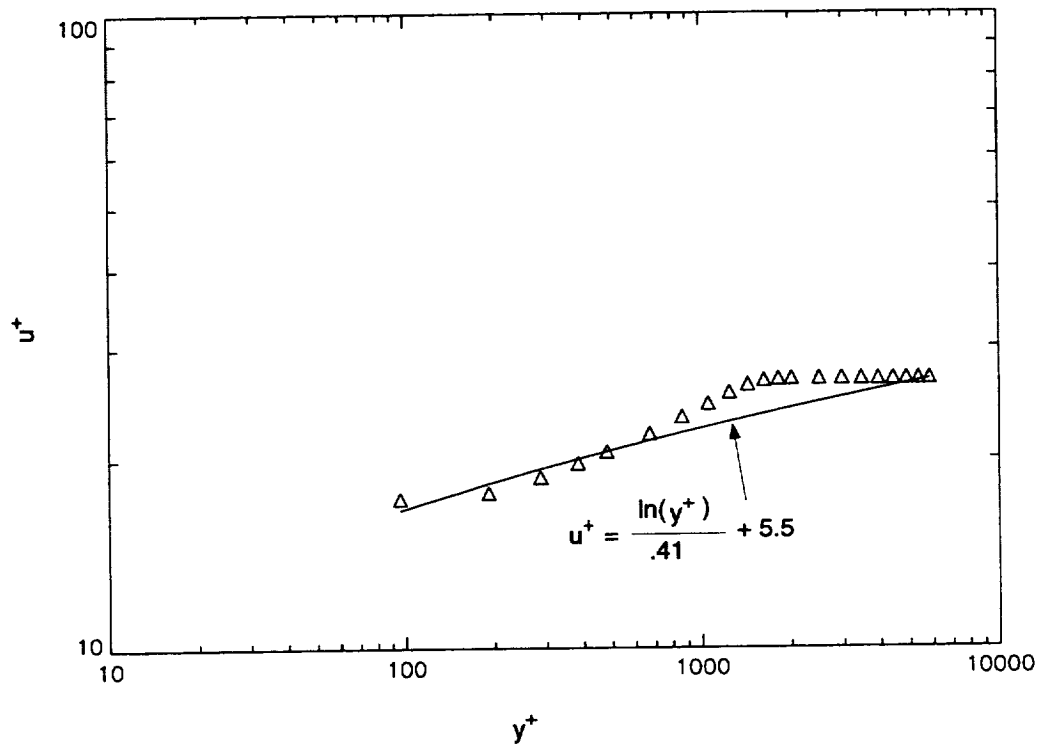


Figure V.2 Experimental law-of-the-wall velocity profile measured near bottom wall 3 inches upstream of diffuser inlet

$$u^+ = \frac{1}{0.41} \ln(y^+) + 5.5 \quad (\text{V.4})$$

The value of $H = 1.52$ for the shape factor is somewhat higher than that of a typical turbulent boundary layer, which is $H = 1.4$. However, because the data agreed with the turbulent law-of-the-wall equation, and the value was well below that for a laminar boundary layer, $H = 2.3$, it was assumed that the boundary layer was turbulent. The difference in shape factor values was attributed to the fact that the probe diameter was 12% of the boundary layer thickness. This made it difficult to get accurate readings in the boundary layer.

The total pressure distribution was uniform over the entire inlet plane, except for in the boundary layer. Secondary flows in the inlet plane were found to be below the resolution

of the probe ($<1^\circ$). This is consistent with other studies of flow in rectangular ducts, where the secondary velocities were found to be only 1% of the axial velocity [22].

Prior to the construction of the modified Internal Fluid Mechanics Facility, some analysis was done to predict the inlet flow conditions. The one-dimensional compressible flow equations were solved in the contraction sections in order to determine the Mach number, static to total pressure ratio, and pressure gradient in the inlet portion of the facility. Plots of the Mach number, static to total pressure ratio and pressure gradient can be seen in Figure V.3. The pressure gradient was determined by taking a central difference of the static pressure at each point along the contraction. The units on pressure gradient are pounds per square inch per inch.

The primary quantity of interest from the one dimensional inlet calculations was the pressure gradient, because it has a strong influence on boundary layer thickness. Since the boundary layer exiting the contraction is small due to the strong pressure gradient involved, it was assumed that a fairly accurate approximation could be made by modeling the boundary layer growth as if it were the same as the boundary layer on a flat plate that

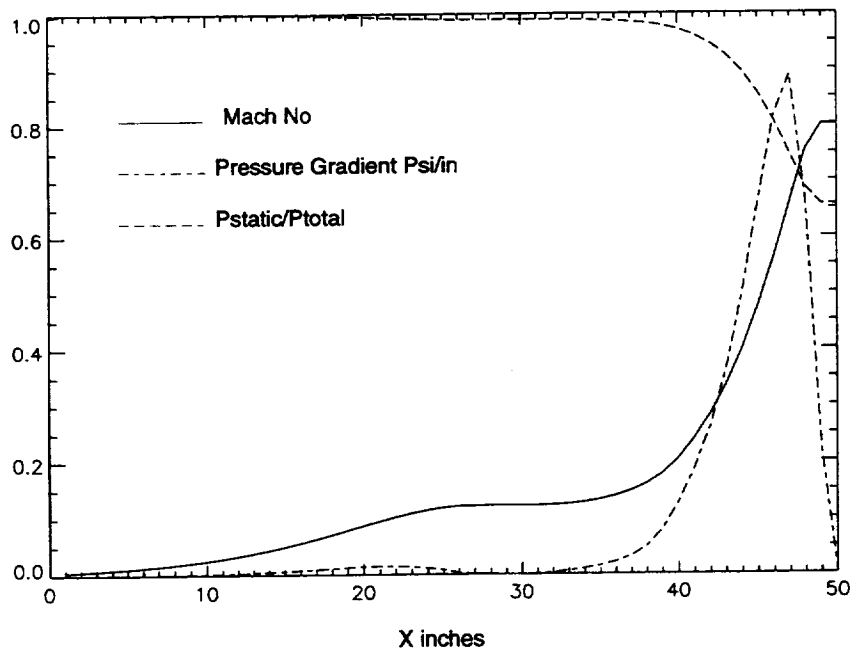


Figure V.3 Flow Characteristics in Contraction Sections

started at a point one inch upstream of the nozzle exit. This point was chosen, because there was little curvature in the last inch of the nozzle and the one dimensional calculation of pressure gradient indicates that the pressure gradient is rapidly approaching zero for the last inch of the contraction, which would allow the boundary layer to begin growing. The equation used was $\delta = \frac{.370x}{Re_x^{1/5}}$ [23]. Where x is a distance along the plate, δ is the boundary layer height, and Re_x is the Reynolds number based on x . This equation is for turbulent flow over a flat plate with Reynolds number calculated with respect to a distance measured in the streamwise direction. A length of four inches was used which is the distance from one inch upstream of the nozzle exit to the measurement plane. With this approximation a value of $\delta = .080$ inches was predicted as the boundary layer height at the plane where inlet flow data were taken. This value matches the measurements taken by the boundary layer probe. By extending the calculation to the actual inlet of the diffuser the boundary layer height at the diffuser inlet was approximated at $\delta = .125$ inches.

CHAPTER VI RESULTS AND DISCUSSION

All data presented in this chapter are in nondimensional form. Aerodynamic results represent time average (probe average) values of measurements. Total pressure is presented as a ratio of the local total pressure and the reference total pressure at the inlet of the diffuser, Equation VI.1. Static pressure is represented by a static pressure coefficient Equation VI.2. The pressures p_o and p represent local values of total and static pressures. Inlet centerline conditions define the reference states $p_{o,cl}$ and p_{cl} . The velocity vectors were nondimensionalized by the cross section average axial velocity at the diffuser exit, as shown in Equation VI.3.

$$C_{p_o} = \frac{p_o}{p_{o,cl}} \quad (VI.1)$$

$$C_p = \frac{p - p_{cl}}{p_{o,cl} - p_{cl}} \quad (VI.2)$$

$$V = \frac{\mathbf{V}}{U_{avg}} \quad (VI.3)$$

For purposes of explaining where various flow phenomena occur in the diffuser, in this section the three distinct surfaces in the diffuser will be referred to as the ramp, centerbody, and cowl. The ramp is the portion of the lower surface of the diffuser that has only two dimensional curvature. The centerbody is the axisymmetric portion of the lower surface of the diffuser that is faired into the hub of the compressor. The cowl is the upper surface of the diffuser. These three surfaces can be seen in Figure VI.1

Flow through Baseline Diffuser

Surface oil visualization, surface static pressure, and five hole probe data were taken for the baseline diffuser case.

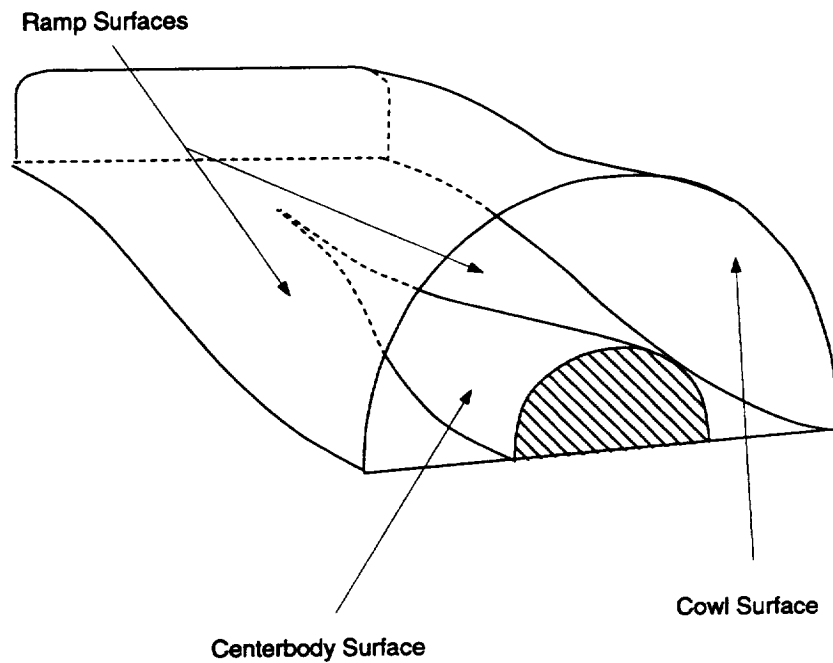


Figure VI.1 Sketch depicting the three distinct surfaces present in the duct

Oil Flow Visualization

A photograph of the streaklines from surface oil visualization can be seen in Figure VI.2. The streaklines on the ramp confirmed that flow through the duct was symmetric. Identical patterns were seen on each side of the centerbody and on each ramp surface. Although not shown here the streakline patterns on the cowl surface were also symmetric. The streaklines on the ramp also indicated a large region of separated flow covering most of the ramp surface on either side of the centerbody. This region began at $x/D = 0.7$ and ended at $x/D = 1.7$. No evidence of separated flow was observed on the cowl surface.

In the tracing of the flow visualization shown in Figure VI.3 boundary layer cross flows can be seen in several areas of the duct. Strong boundary layer crossflows can be seen on either side of the centerbody near $x/D = 1.25$. Cross flows are also present in the corner between the ramp and the cowl surfaces. This crossflow ends at a stagnation line between the ramp/cowl corner and the region of separation. Near the exit plane boundary layer cross flows can be seen on the ramp near the centerbody, indicating that the centerbody is forcing fluid towards the outside corners of the diffuser, preventing separation from occurring there.



Figure VI.2 Photograph of surface oil flow visualization

Surface Static Pressure Measurements

The axial distribution of static pressure is shown in Figure VI.4. For the first several measurements the static pressure actually drops, despite a small increase in the area of the duct. This could indicate that the growth of the boundary layer is offsetting the increase in duct area. However, it is most likely caused by the streamline curvature at the inlet. As the duct area continues to expand the static pressures on all surfaces begin to rise. The static pressure on the cowl rises faster than the pressure on either the ramp or bottom centerline. Just upstream of the point of separation the static pressure on the cowl is higher than on the ramp or centerbody. The static pressure along the bottom centerline begins to rise more quickly than the pressure on the ramp surface as the centerbody becomes larger, after $x/D = 0.5$. Around $x/D = 0.8$ the effect of the centerbody is seen on the ramp surface, and the static pressure on the ramp begins to rise. Consequently, by the middle of the duct,

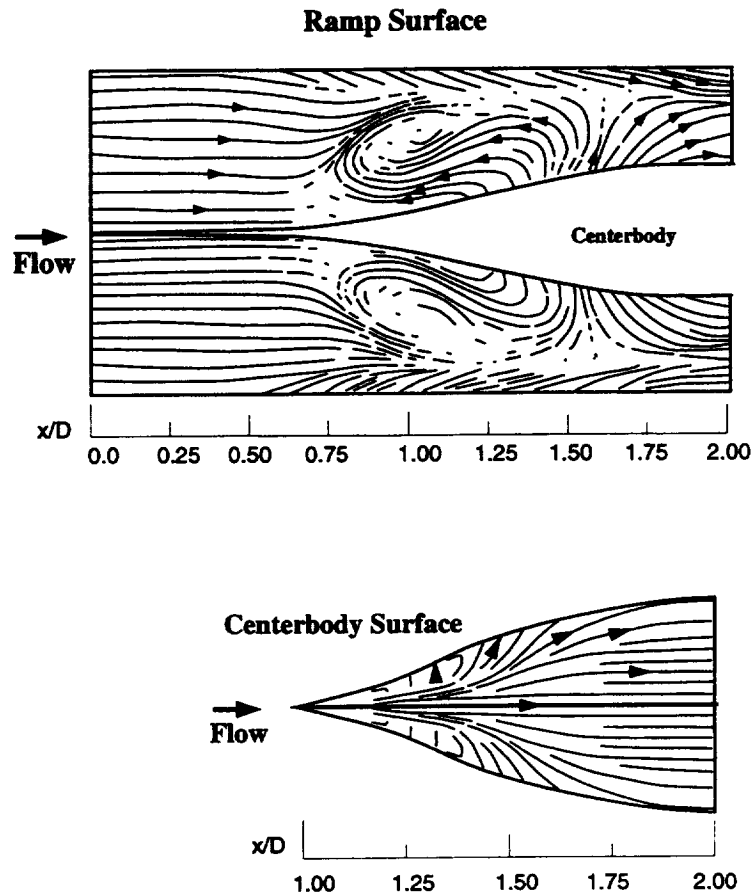


Figure VI.3 Tracing of surface oil flow visualization

$x/D = 1.0$, the static pressures on the three axial lines are roughly equal. As the size of the centerbody increases, the static pressure in the center of the bottom of the duct also increases. This causes the boundary layer crossflows that can be seen on the sides of the centerbody as surface air flows from the centerbody to the surface of the ramp, according to the surface flow visualization streaklines.

The distribution of axial static pressure measurements on the cowl centerline are similar to those calculated by Anderson and Kapoor [4]. The shape of the curves are very similar. However, in the region of separated flow the static pressures measured seem to rise more slowly than predicted. There is some difference in the actual values at all positions. This is most likely due to uncertainty in the reference pressures.

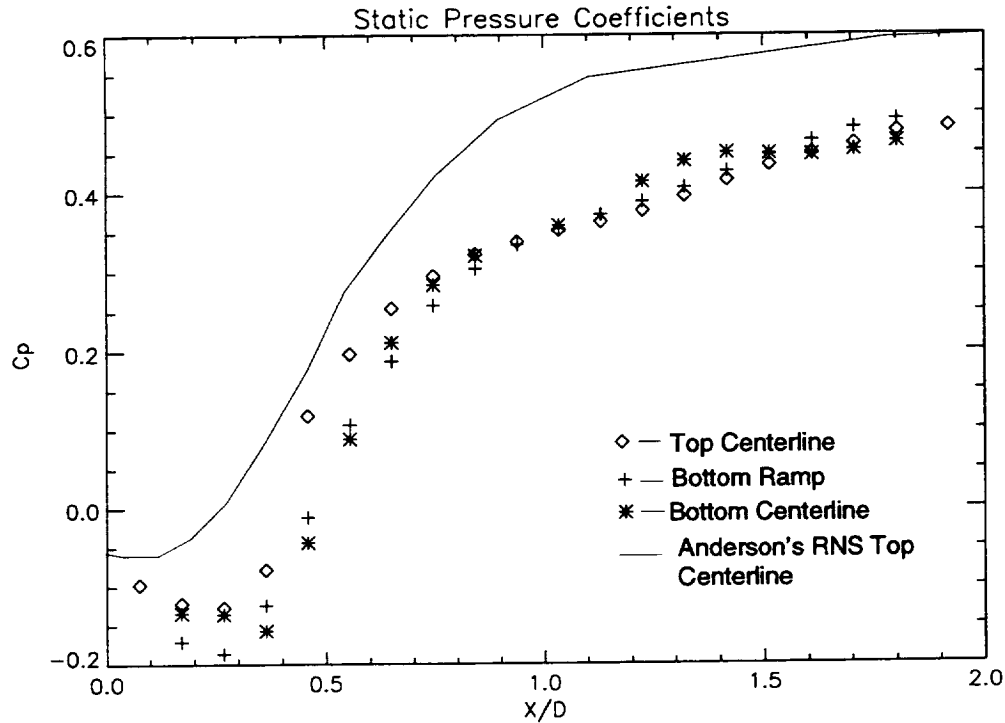


Figure VI.4 Static pressure coefficients in axial direction

Circumferential lines of static pressure were measured at three locations in the duct $x/D = .2, 1.0, 1.8$. Plots of these can be seen in Figure VI.5. At all three locations static pressure is roughly equal throughout the duct. There is a slight variation at the first line of static pressures. By the second row of circumferential taps the pressures are equal around the entire duct. The same is true of the third row.

Five Hole Probe Data

The total pressure distribution at the exit plane is shown in Figure VI.6. The primary regions of higher total pressure loss are clearly identified. The curvature of the ramp generated a large adverse pressure gradient. This large adverse pressure gradient was responsible for the region of flow separation on the ramp surface. The area averaged total pressure recovery of the duct was $p_o/p_{ref} = .951$. As with the static pressure, this result is very close to that found in the study by Anderson and Kapoor, which was $p_o/p_{ref} = .960$. The maximum circumferential distortion was characterized by an intensity of .074, with an extent of 51.4 degrees, and a multiple-per-rev quantity of 2.0.

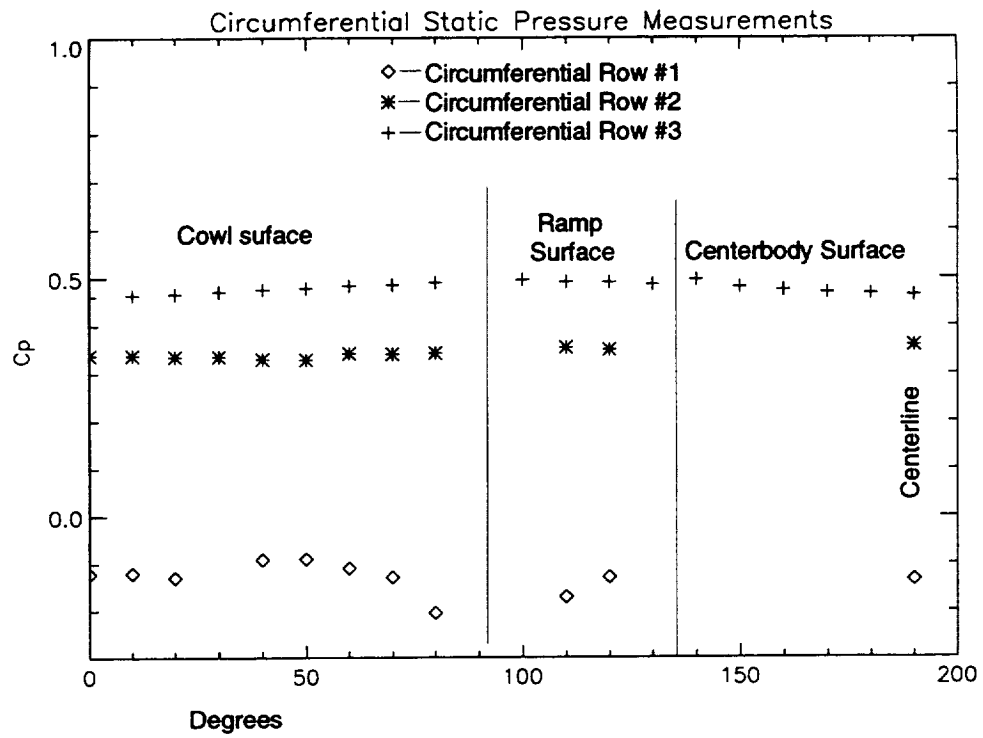


Figure VI.5 Circumferential static pressure coefficients

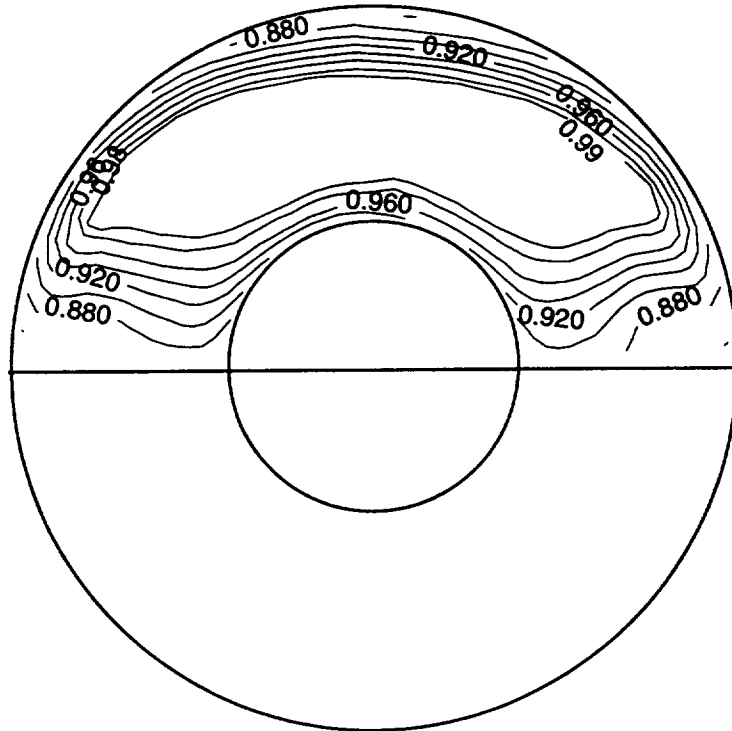


Figure VI.6 Total pressure contours for baseline case

The cross flow velocities in exit plane are shown in Figure VI.7. Several conclusions can be drawn from these data. First, the results are symmetric. The largest difference between the two sides of the duct are the large vectors pointed toward the cowl near the cowl surface that are visible on only one side, and not the other. This is most likely due to the effect of the wall on one of the probes, and does not necessarily indicate a difference in the flow field from one half of the duct to the other.

The most pronounced feature of the secondary velocity plot is the vortical flow that is present just above the ramp surface. This vortical flow was due to flow near the ramp surface being forced away from the centerline of the diffuser by the centerbody, and the flow near the cowl surface being forced toward the centerline of the diffuser by the cowl corner transition.

Comparison with the computational work done by Anderson and Kapoor show that neither the Reduced Navier Stokes (RNS) nor the Full Navier Stokes (FNS) solutions correctly predicted the velocities at the exit of the duct [4]. For the RNS solution the vortices near the ramp surface, and the centerbody appear to be in the nearly same places in both the test data and the computational results. However, the vortex structure in the data appears weaker than that predicted by the computer model, particularly in the corners (See Figure VI.9). This difference is even more pronounced in the full Navier-Stokes solution. In that solution the vortices are much tighter and display much less diffusion than was found to be the case in the actual duct. Also in that solution the axial velocity contours display circular characteristics caused by these vortices (Figure VI.10). These circular patterns were not seen in the data (Figure VI.8). It is possible that these incorrect velocity vectors are a result of a problem in the turbulence model. Anderson and Kapoor noted that the FNS solutions were very sensitive to the "F" function used in the Baldwin-Lowmax turbulence model.

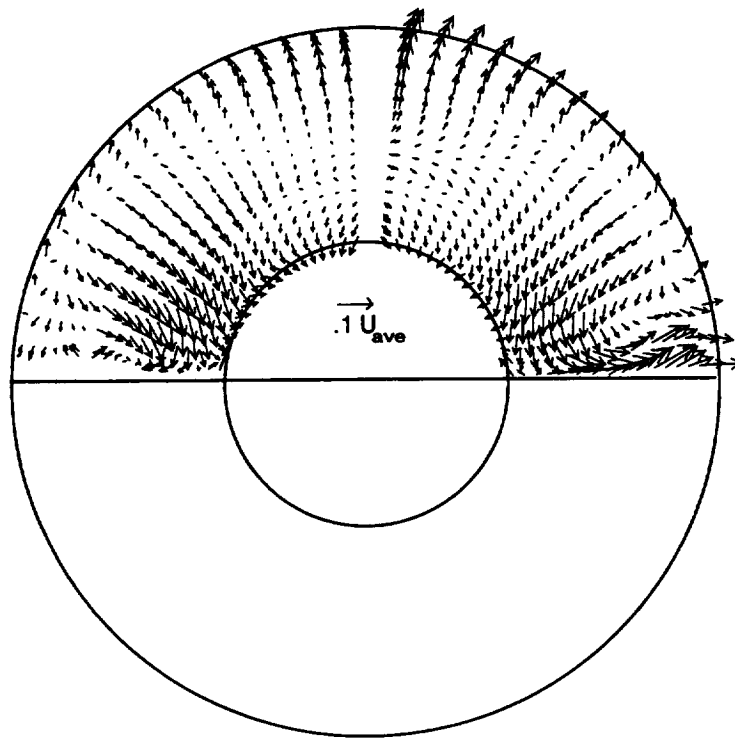


Figure VI.7 Cross flow velocities at exit plane for baseline case

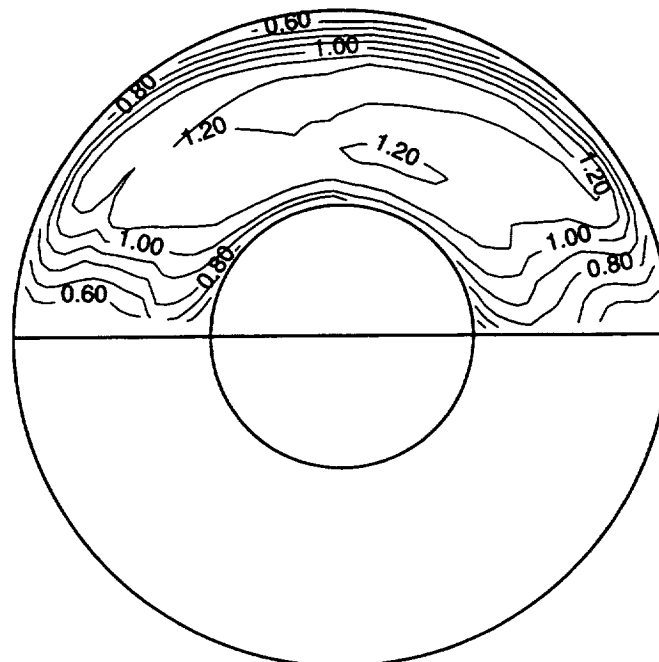
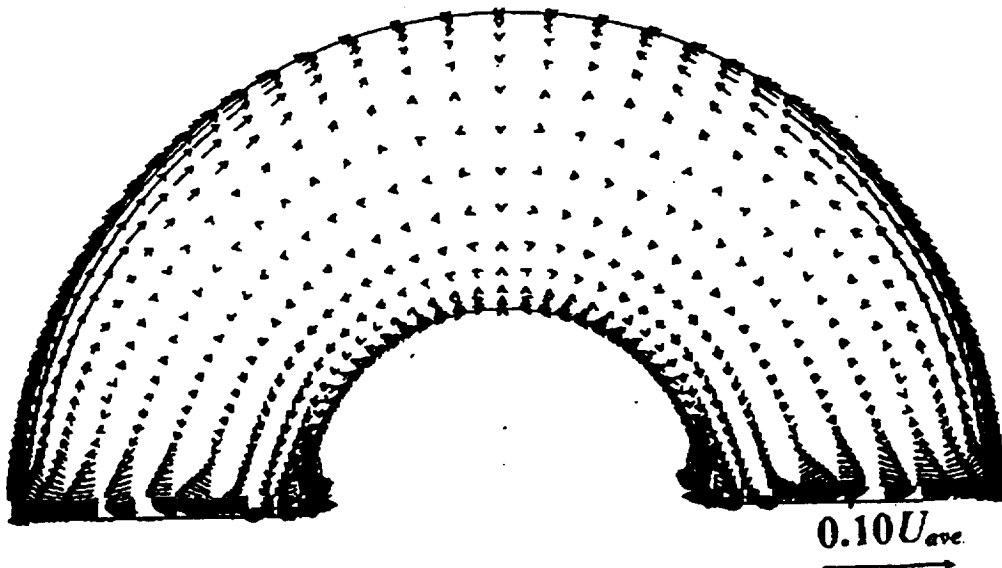
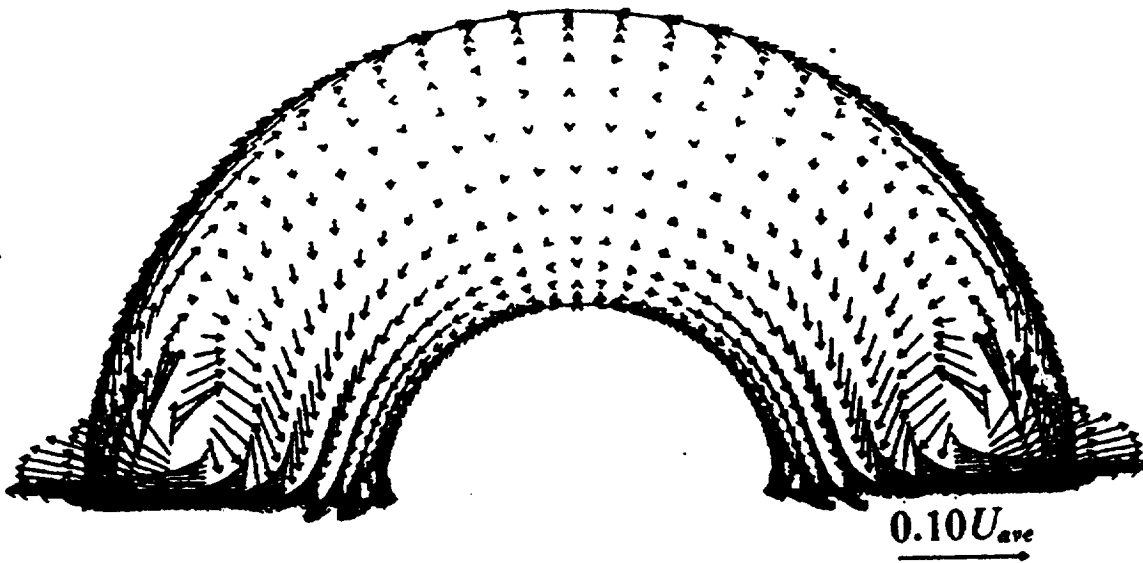


Figure VI.8 Axial velocities measured at AIP for baseline case

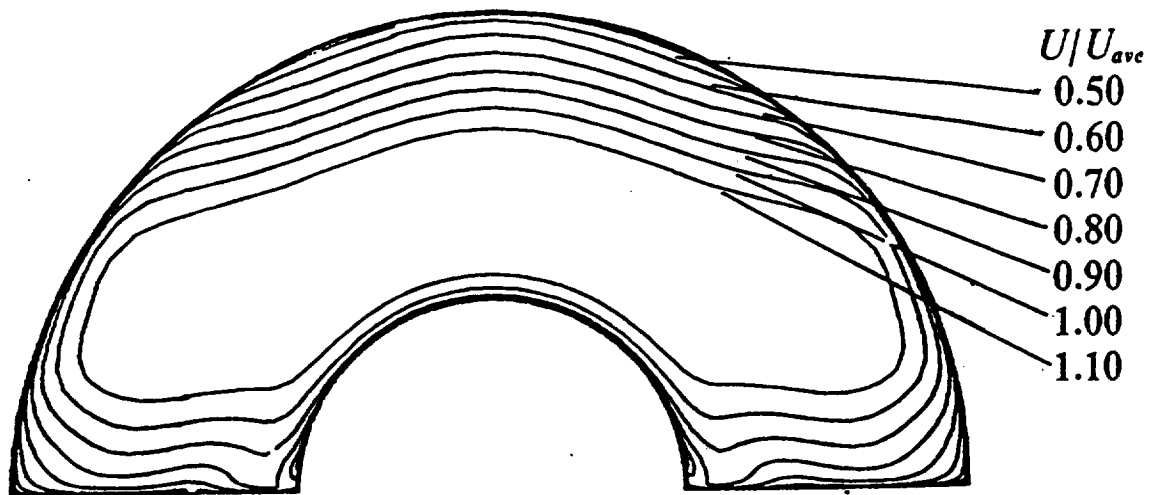


(a) Reduced Navier-Stokes Analysis

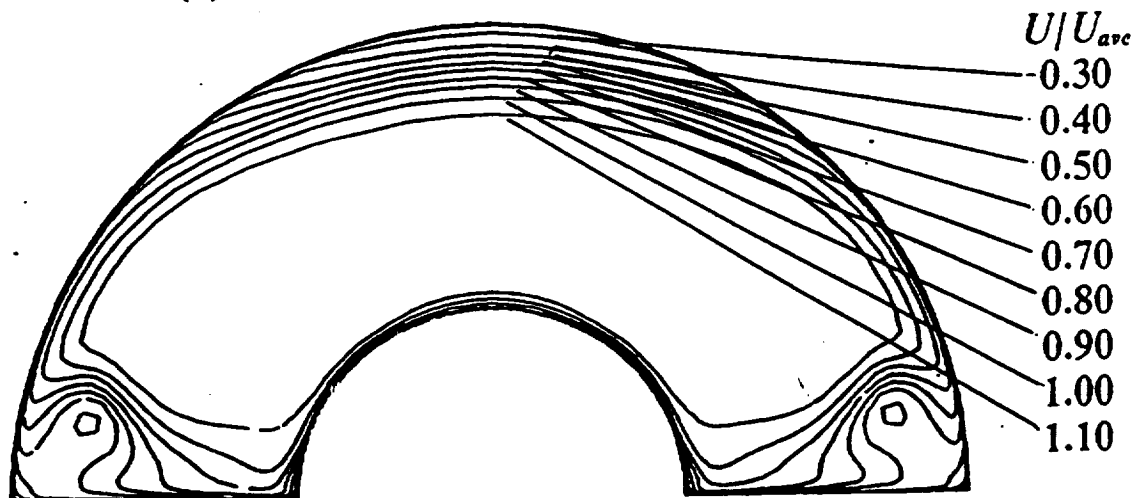


(b) Full Navier Stokes Analysis

Figure VI.9 Anderson and Kapoor's computation of transverse velocities a) Reduced b) Full Navier Stokes Analysis



(a) Reduced Navier-Stokes Analysis



(b) Full Navier Stokes Analysis

Figure VI.10 Anderson and Kapoors computation of axial velocities a) Reduced b) Full Navier Stokes Analysis

Effect of Vortex Generators

For the case of the baseline diffuser with vortex generators surface oil visualization, and five hole probe data were acquired.

Surface Oil Flow Visualization

Tapered fin vortex generators were used to eliminate the region of separated flow. By moving boundary layer flow away from the area of separation, continuity compels higher momentum fluid from the mean flow towards the ramp surface of the diffuser. This action combined with the mixing activity of the vortices caused the flow behind the vortex generators to remain attached, where that flow was separated in the baseline case. This is demonstrated by the large area of attached flow shown in Figure VI.11 which replaced the large region of separated flow there previously. Some separated flow still exists on either side of the vortex pair. The long stagnation line between the corner of the cowl and ramp surfaces and the vortex is most likely caused by the combined upflow of the vortex from the vortex generator and the flow away from the wall that was present for both the baseline duct and the configuration with vortex generators. The upflow from the vortex generator near the centerbody can be seen from the point where the vortex impacts the centerbody to the exit plane.

Five Hole Probe Data

The total pressure recovery for the duct with vortex generators was $p_o/p_{ref} = .948$ (see Figure VI.12). The fact that the pressure recovery of the duct does not increase, with the elimination of the large separated region on the ramp surface indicates that the region of separation is relatively thin, and thus has little effect on pressure recovery. The maximum circumferential distortion was characterized by an intensity of .0534, with an extent of 52.3 degrees, and a multiple-per-rev value of 2.0. This is much better than in the duct without vortex generators.

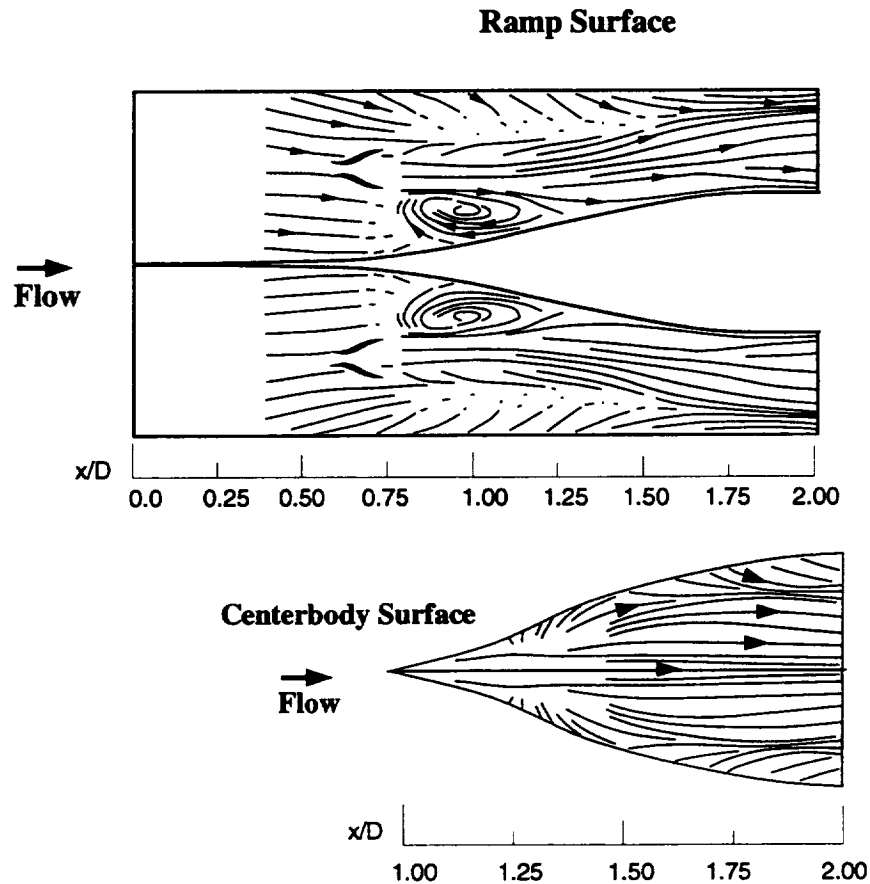


Figure VI.11 Surface oil flow visualization behind vortex generators

The distortion parameters can be used as a tool to better understand total pressure recovery, and why the vortex generators didn't improve the overall total pressure recovery much, despite substantially reducing the amount of flow separation in the duct. In Figure VI.13 the difference in the distortion intensities between the baseline duct and the duct with vortex generators can be seen. With the vortex generators in place the distortion intensity was lower across the entire face of the diffuser exit. However, the plot of the extent of the distortion (Figure VI.14) shows that the circumferential distance covered by low total pressure fluid is much larger for the case with vortex generators. A major cause of this appears to be the impingement of the generated vortices on the centerbody, forcing low momentum fluid up the surface of the centerbody towards the higher momentum mean flow.

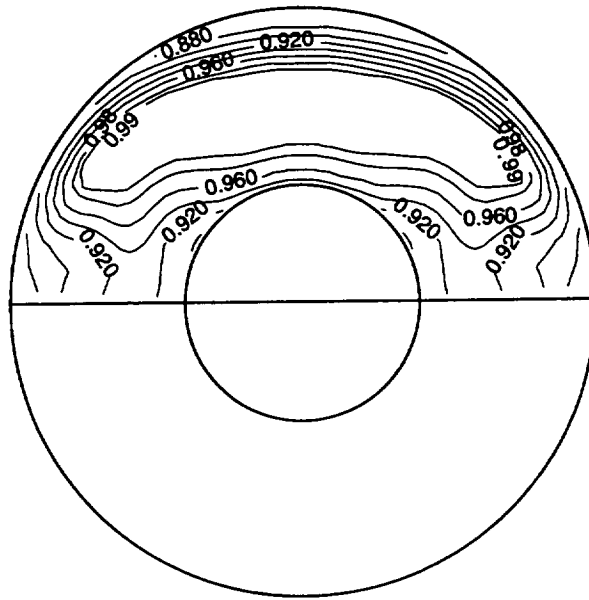


Figure VI.12 Total pressure contours with vortex generator array

As Figures VI.13 and VI.14 show, the vortex generators reduced the intensity of the distortion at each radial position by moving the regions of low total pressure around. This was particularly true about the region near the centerbody where low momentum fluid was pushed up into the mean flow by the interaction of the generated vortices with the centerbody.

The plot of the secondary velocities in Figure VI.15 shows where the generated vortices appeared in the exit plane. The vortices can be seen on the ramp surface in the center of the ramp, and next to the centerbody. Both of the vortices created by the generators followed the ramp surface of the duct from the vortex generators to the exit plane. Neither convected up into the mean flow. The vortex near the centerbody apparently followed the surface of the centerbody to the exit plane. Several vectors pointed away from the ramp surface along the surface of the centerbody can be seen. Flow in the same direction was seen in the surface flow visualization on the centerbody. The axial velocity was higher near the center of the ramp surface for the case (Figure VI.16). This is evidence of the redistribution of the total pressure distortion from circumferential to radial that was evident in the total pressure data as well.

Distortion Parameter Across Engine Face

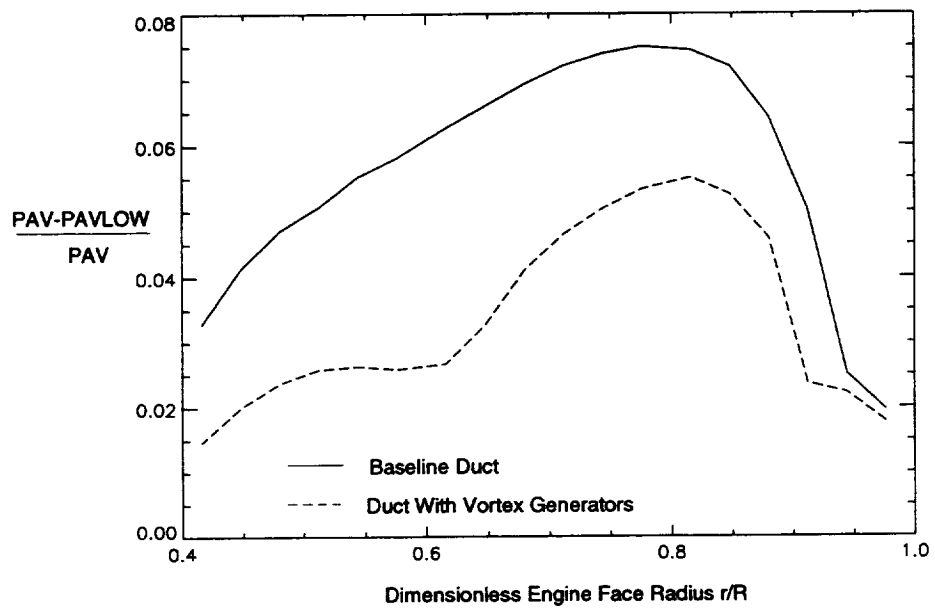


Figure VI.13 Distortion intensity

Distortion Extent Across Engine Face

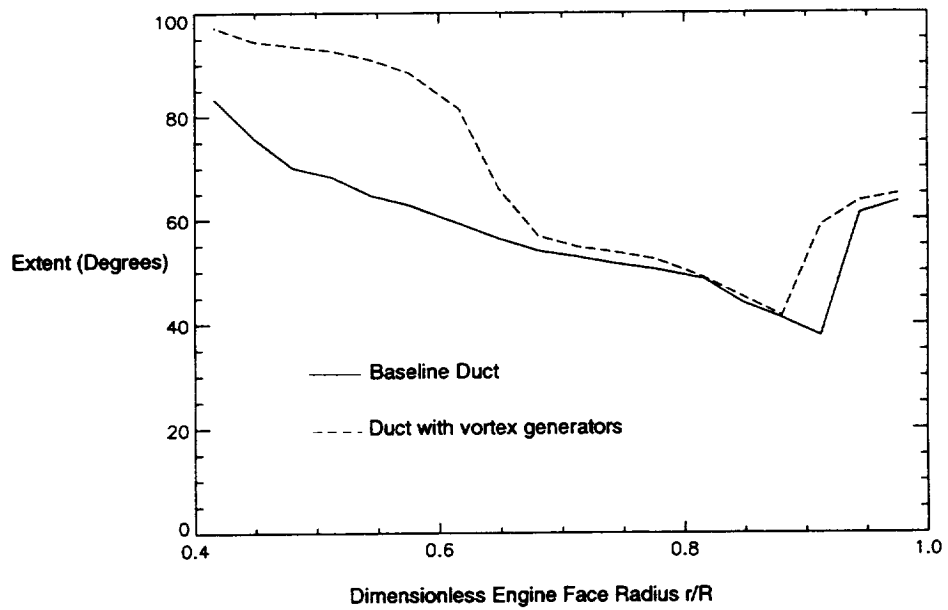


Figure VI.14 Distortion extent

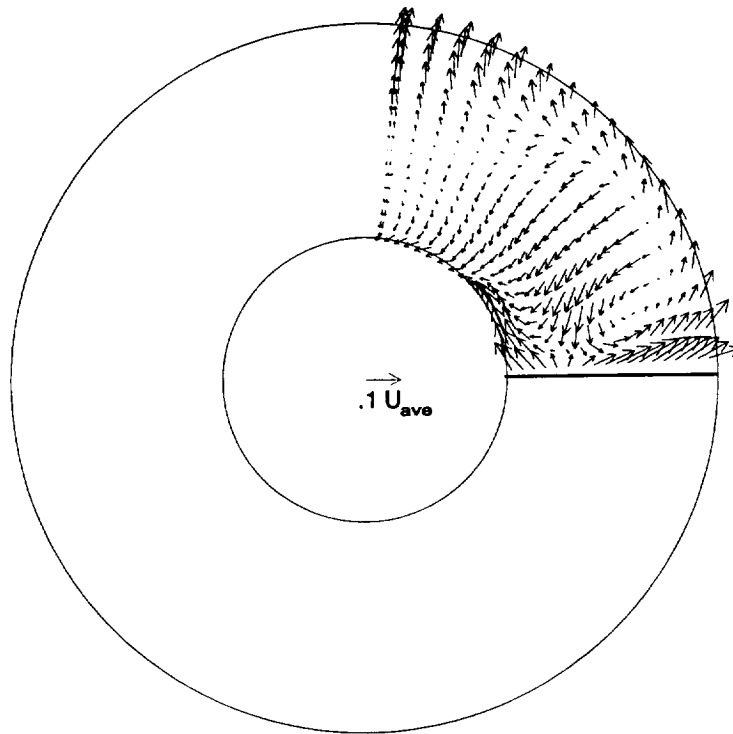


Figure VI.15 Secondary velocities at exit plane with vortex generators

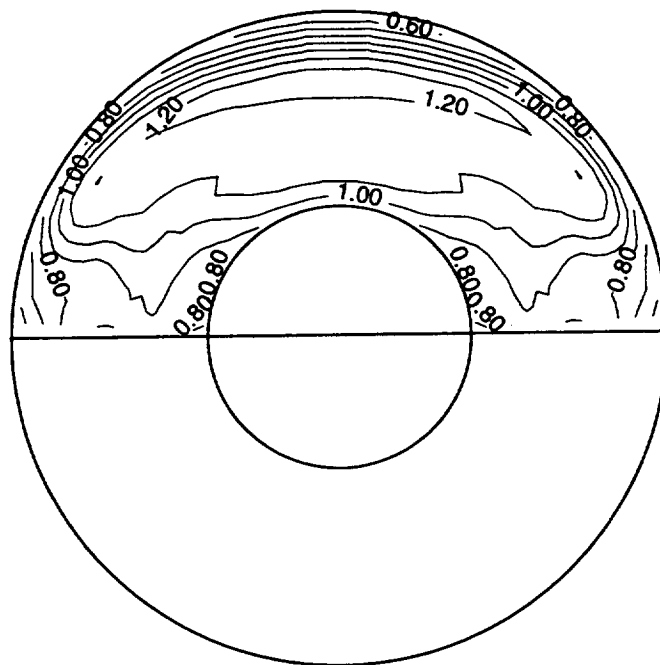


Figure VI.16 Axial velocity with vortex generators

CHAPTER VII CONCLUSIONS

Flow through a rectangular-to-semiannular diffuser was studied. Baseline aerodynamic measurements were taken to quantify the three dimensional velocity vectors, and the total pressure distributions at the inlet and exit of the diffuser. Surface static pressure measurements were also taken, and surface flow visualization were acquired.

A large region of separated flow was observed on the ramp surface of the duct. This was caused by the large curvature and thus adverse pressure gradient associated with that surface of the diffuser. This curvature was also responsible for a large region of low momentum fluid that was present at the exit plane of the duct. The centerbody functioned as a flow pushing device that helped prevent separation in the corners. The cross flow angles at the exit of the duct were found to be relatively small. In general, the experimental results compared well with previous computational work done at NASA. The computational results did not, however, predict flow separation on the ramp surface.

A test to determine the effect of vortex generators on the performance of the duct was completed. The vortex generators eliminated a large portion of the separated flow on the ramp surface. The total pressure recovery was not improved appreciably by the vortex generators, but circumferential total pressure distortion was improved substantially. However, the extent of the circumferential distortion increased near the centerbody, due to low momentum fluid being pushed up the cowl and centerbody surfaces.

Modifications to the Internal Fluid Mechanics Facility at NASA-Lewis to make it available for HSR diffuser tests were also completed. These modifications performed as expected. Good flow quality was achieved in the test section. Also the efficiency of the facility was improved, due to the new instrumentation duct that was specifically designed to handle the probes used in this study.

CHAPTER VIII

RECOMMENDATIONS FOR FURTHER RESEARCH

Further research needs to be done in order to completely understand the flow in this transition diffuser. While the data presented in this thesis provides a complete analysis of the diffuser performance, more detailed studies would be helpful. With a sturdier diffuser wall, measurements could be taken at intermediate axial positions in order to determine the height of the region of separated flow. An ethylene trace gas analysis of the flow field would be helpful in determining the effect of the centerbody with regards to flow pushing, and the effect of the flow separation. Also the development of a tool that would allow flow visualization data to be transferred into a three dimensional computer model would be helpful, because the many different surfaces on this duct make two dimensional representations of the data difficult to interpret.

A detailed vortex generator study would be very helpful in determining if it is possible to improve diffuser performance with such devices. A more complete vortex generator study including different numbers and sizes of vortex generators, as well as different placement schedules would be very useful. Also a computational study of the use of vortex generators in this and other diffusers would be useful.

A study of a duct with this geometry in a facility capable of producing supersonic flow upstream of the diffuser inlet would allow for a study of the unsteady characteristics of the total pressure distortion. In that same facility a test which varies the Reynolds number could be conducted. This would be helpful in determining, what, if any, effects Reynolds number variation has on flow separation in inlets of this type. Studies with different inlet boundary layer heights should also be done in order to determine the effect of inlet boundary layer thickness on duct performance.

Finally, as part of the ongoing development of the High Speed Civil Transport, whole other diffuser geometries must be tested.

BIBLIOGRAPHY

- [1] Anderson, B. H., "Three-Dimensional Viscous Design Methodology of Supersonic Inlet Systems for Advanced Technology Aircraft," *Numerical Methods for Engine-Airframe Integration*, edited by S. N. B. Murthy and G. C. Paynter, AIAA, 1986, pp. 431-480.
- [2] Seddon, J. and Goldsmith, E., *Intake Aerodynamics*, AIAA Education Series, American Institute of Aeronautics and Astronautics, Inc., Washington, D.C., 1985.
- [3] Brown, A. C., "Subsonic Diffusers Designed Integrally with Vortex Generators," *Journal of Aircraft*, Vol. 5, 1968, pp. 221-229.
- [4] Anderson, B. and Kapoor, K., "A Study on Bifurcated Transitioning S-Ducts for High Speed Inlet Application," AIAA paper 94-2812, 1994.
- [5] Mealson, E., Burstadt, P., and Wasserbauer, J., "Experimental Investigation of the Performance of a Mach 2.7 Two Dimensional Bifurcated Duct Inlet with 30 Percent Internal Contraction," Internal NASA Report tech. rep., 1993.
- [6] Hercock, R. and Williams, D., "Aerodynamic Response," *Distortion Induced Engine Instability*, AGARD, 1975.
- [7] Lotter, K. and Scherbaum, R., "A Novel High-Performance System for Recording and Analysing Instantaneous Total Pressure Distortion in Air Intakes," *Aerodynamic Engine/Airframe Integration for High Performance Aircraft and Missiles*, AGARD, 1993.
- [8] Bowditch, D. N. and Coltrin, R. E., "A survey of Inlet/Engine Distortion Compatibility," NASA TM 83421, 1983.
- [9] "Gas Turbine Engine Inlet Flow Distortion Guidelines," Society of Automotive Engineers ARP 1420, Mar. 1978.
- [10] "Inlet Total-Pressure-Distortion Considerations for Gas-Turbine Engines," Society of Automotive Engineers AIR 1419, May 1983.

- [11] A.R. Porro, C. W. W.R. Hingst and Andrews, T., "The NASA Lewis Research Center Internal Fluid Mechanics Facility," NASA TM 105187, 1991.
- [12] Misu, I., Okamoto, T., and Kai, Y., "Reverse Transition of Turbulent Corner Flow in Contraction of Rectangular Sections," *Trans. Japan Soc. Aero. Space Sci.*, Vol. 28, no. 82, 1986, pp. 219–229.
- [13] Morel, T., "Comprehensive Design of Axisymmetric Wind Tunnel Contractions," *Journal of Fluids Engineering*, Vol. 97, June 1975, pp. 225–233.
- [14] Su, Y., "Flow Analysis and Design of Three-Dimensional Wind Tunnel Contractions," *AIAA Journal*, Vol. 29, Nov. 1991, pp. 1912–1920.
- [15] Okamoto, T. and Misu, I., "Reverse Transition of Turbulent Boundary Layer on Planar Wall of Two-Dimensional Contraction," *Trans. Japan Soc. Aero. Space Sci.*, Vol. 20, 1977.
- [16] White, F. M., *Viscous Fluid Flow*, second ed., McGraw-Hill Series in Mechanical Engineering, McGraw-Hill, Inc., New York, 1991.
- [17] Sreenivasan, K., "Laminarizing, Relaminarizing and Retransitional Flows," *Acta Mechanica*, Vol. 44, 1982, pp. 1–48.
- [18] Reichert, B. A. and Wendt, B. J., "Improving Diffusing S-Duct Performance by Secondary Flow Control," AIAA Paper 94-0365, 1994. (Also NASA TM 106492).
- [19] Wellborn, S. R., Okiishi, T. H., and Reichert, B. A., "A Study of the Compressible Flow Through a Diffusing S-Duct," NASA TM 106411, Dec. 1993.
- [20] Reichert, B. A. and Wendt, B. J., "Uncertainty of Five-Hole Probe Measurements," *Fluid Measurement and Instrumentation 1994*, edited by T. B. Morrow, G. L. Morrison, and R. A. Gore, American Society of Mechanical Engineers, New York, NY, 1994, pp. 39–44.

- [21] Krause, L. N. and Gettleman, C. C., "Effect of Interaction Among Probes, Supports, Duct Walls and Jet Boundaries on Pressure Measurements in Ducts and Jets," *ISA Proceedings*, Vol. 7, ISA, 1952, pp. 138–146.
- [22] Melling, A. and Whitelaw, J., "Turbulent Flow in a Rectangular Duct," *Journal of Fluid Mechanics*, Vol. 78, 1976, pp. 289–315.
- [23] Munson, B. R., Young, D. F., and Okiishi, T. H., *Fundamentals of Fluid Mechanics*, 1st ed., John Wiley and Sons, Inc., New York, 1990.

REPORT DOCUMENTATION PAGE			Form Approved OMB No. 0704-0188	
Public reporting burden for this collection of information is estimated to average 1 hour per response, including the time for reviewing instructions, searching existing data sources, gathering and maintaining the data needed, and completing and reviewing the collection of information. Send comments regarding this burden estimate or any other aspect of this collection of information, including suggestions for reducing this burden, to Washington Headquarters Services, Directorate for Information Operations and Reports, 1215 Jefferson Davis Highway, Suite 1204, Arlington, VA 22202-4302, and to the Office of Management and Budget, Paperwork Reduction Project (0704-0188), Washington, DC 20503.				
1. AGENCY USE ONLY (Leave blank)	2. REPORT DATE April 1995	3. REPORT TYPE AND DATES COVERED Final Contractor Report		
4. TITLE AND SUBTITLE Study of Compressible Flow Through a Rectangular-to-Semiannular Transition Duct		5. FUNDING NUMBERS WU-505-62-52 G-NAG3-1561		
6. AUTHOR(S) Jeffry Foster, Theodore H. Okiishi, Bruce J. Wendt, and Bruce A. Reichert				
7. PERFORMING ORGANIZATION NAME(S) AND ADDRESS(ES) Iowa State University Ames, Iowa 50011		8. PERFORMING ORGANIZATION REPORT NUMBER E-9582		
9. SPONSORING/MONITORING AGENCY NAME(S) AND ADDRESS(ES) National Aeronautics and Space Administration Lewis Research Center Cleveland, Ohio 44135-3191		10. SPONSORING/MONITORING AGENCY REPORT NUMBER NASA CR-4660		
11. SUPPLEMENTARY NOTES Project Manager, John M. Abbott, Internal Fluid Mechanics Division, NASA Lewis Research Center, organization code 2660, (216) 433-3607.				
12a. DISTRIBUTION/AVAILABILITY STATEMENT Unclassified - Unlimited Subject Category 07 This publication is available from the NASA Center for Aerospace Information, (301) 621-0390.		12b. DISTRIBUTION CODE		
13. ABSTRACT (Maximum 200 words) Detailed flow field measurements are presented for compressible flow through a diffusing rectangular-to-semiannular transition duct. Comparisons are made with published computational results for flow through the duct. Three-dimensional velocity vectors and total pressures were measured at the exit plane of the diffuser model. The inlet flow was also measured. These measurements were made using calibrated five-hole probes. Surface oil flow visualization and surface static pressure data were also taken. The study was conducted with an inlet Mach number of 0.786. The diffuser Reynolds based on the inlet centerline velocity and the exit diameter of the diffuser was 3,200,000. Comparison of the measured data with previously published computational results are made. Data demonstrating the ability of vortex generators to reduce flow separation and circumferential distortion is also presented.				
14. SUBJECT TERMS Engine inlets; Inlet flow; Intake systems		15. NUMBER OF PAGES 61		
		16. PRICE CODE A04		
17. SECURITY CLASSIFICATION OF REPORT Unclassified	18. SECURITY CLASSIFICATION OF THIS PAGE Unclassified	19. SECURITY CLASSIFICATION OF ABSTRACT Unclassified	20. LIMITATION OF ABSTRACT	

